Rotor-bearing system integrated with shape memory alloy springs for ensuring adaptable dynamics and damping enhancement-Theory and experiment

Enemark, Søren; Santos, Ilmar F.

Published in:
Journal of Sound and Vibration

Link to article, DOI:
10.1016/j.jsv.2016.01.023

Publication date:
2016

Document Version
Peer reviewed version

Rotor-bearing system integrated with shape memory alloy springs for ensuring adaptable dynamics and damping enhancement – Theory and experiment

Søren Enemark[a], Ilmar F Santos[a,*]

[a]*Department of Mechanical Engineering, Technical University of Denmark, Nils Koppels Allé, building 404, DK-2800 Kgs. Lyngby, Denmark*

Abstract

Helical pseudoelastic shape memory alloy (SMA) springs are integrated into a dynamic system consisting of a rigid rotor supported by passive magnetic bearings. The aim is to determine the utility of SMAs for vibration attenuation via their mechanical hysteresis, and for adaptation of the dynamic behaviour via their temperature dependent stiffness properties. The SMA performance, in terms of vibration attenuation and adaptability, is compared to a benchmark configuration of the system having steel springs instead of SMA springs.

A theoretical multidisciplinary approach is used to quantify the weakly nonlinear coupled dynamics of the rotor-bearing system. The nonlinear forces from the thermo-mechanical shape memory alloy springs and from the passive magnetic bearings are coupled to the rotor and bearing housing dynamics. The equations of motion describing rotor tilt and bearing housing lateral motion are solved in the time domain. The SMA behaviour is also described by the complex modulus to form approximative equations of motion, which are solved in the frequency domain using continuation techniques.

Transient responses, ramp-ups and steady state frequency responses of the system are investigated experimentally and numerically. By using the proper SMA temperature, vibration reductions up to around 50 % can be achieved using SMAs instead of steel. Regarding system adaptability, both the critical speeds, the mode shapes and the modes' sensitivity to disturbances (e.g. imbalance) highly depend on the SMA temperature. Examples show that vibration reduction at constant rotational speeds up to around 75 % can be achieved by changing the SMA temperature, primarily because of stiffness change, whereas hysteresis only limits large vibrations. The model is able to capture and explain the experimental dynamic behaviour.

Keywords: Rotor-bearing dynamics, shape memory alloys, vibration reduction, hysteresis, passive magnetic bearings

1. Introduction

During the last 10 years, incorporation of shape memory alloys (SMAs) into rotating systems has gained increasing attention resulting in a variety of publications in the literature. This is due to the unique characteristics of the material, which can be used in different ways to ease the crossing of critical speeds, enhance damping, suppress instability etc. SMAs are metallic alloys that exhibit different crystallographic phases depending on temperature and stress levels. This means that SMAs have thermo-mechanically dependent stiffness properties (adaptable critical speeds). Also, solid-state transformations between the phases or reorientations within the martensitic phase cause large recoverable deformations (actuation), and significant mechanical hysteresis (damping) [1].

*Corresponding author

As the first, Nagaya et al. [2] suggested to use the actuation principle of SMAs in rotating systems. The on/off SMA actuator was coupled to a stiffness adding device in order to change the critical speeds, such that they could be avoided during run-up or run-down. Later, the idea was experimentally validated, and it was highlighted that the change in critical speed has to be abrupt in order not to excite eigenmodes [3]. Appropriate level of damping is required because abrupt stiffness changes are difficult (if not impossible) to realise. The actuation principle was also used in [4], where SMA actuators changed the pre-tension of a nonlinear elastomer bearing support. Thereby the critical speeds depended on the SMA temperature.

The stiffness of an SMA depends on its temperature. This effect can be used to control the critical speeds of rotor-bearing systems and avoid high level of vibrations. Examples of SMA machine element are composite sleeve-rings [5, 6] and springs [7, 8, 9] combined with either on/off control [5, 6, 7, 8] or continuous control [9] of temperature. In this respect it is necessary to have a relatively compliant bearing in order to be able to make the system adaptable [5]. Push-pull SMA mechanisms (antagonistic action) can be used for increasing the bandwidth of the actuator that is limited by the rate of convection [6]. This is a general obstacle in SMA actuation.

Hybrid approaches have also been proposed, in which both the temperature dependent stiffness as well as the hysteretic damping of the stress-induced transformations are utilised [10, 11]. Alves et al. [10] numerically investigated a flexible rotor with an SMA wire support, where the pseudoelastic SMAs were in pre-tension so that hysteretic damping occurred already at relatively low vibration amplitudes. Similarly, Enemark et al. [11] investigated a system consisting of a dynamically coupled rigid rotor and passive magnetic bearing housings with integrated pseudoelastic SMA helical springs in pre-tension. In both works it was found that the stiffness increases with temperature whereas the damping capabilities diminish. However, Enemark et al. [11] showed experimentally that a rise in temperature could result in a decrease in resonance amplitude even though the level of hysteretic damping reduced, because also the mode shapes change with temperature.

Yet another approach is to use SMAs in backup-bearings, which has been exemplified in form of a discontinuous support [12]. Numerical investigations showed that the dissipative hysteresis effects of the SMAs cause more desirable dynamic behaviour compared to an elastic support. However in a similar investigation of a single degree of freedom impact oscillator, Sitnikova et al. [13] concluded that in some cases the dynamic response complexity actually increases if using SMAs. This means that SMAs are not always beneficial in terms of vibration reduction in such systems.

Ertas et al. [14] investigated the feasibility of using metal mesh dampers made from SMAs, which can be used for engine mounting or vibration absorbers. They found the SMA damping characteristics superior to e.g. copper mesh dampers when vibration amplitudes were larger than 8 μm. Similar SMA mesh washers, or SMA metal rubber, have been suggested to be used as smart rotor support for active vibration control [15, 16]. The stiffness and damping properties were determined to be functions of the environmental temperature, excitation amplitude and frequency, and the loss factor was found to be up to 0.5.

The thermo-mechanical properties of SMAs are nonlinear, which means that they may cause complex dynamics in general, e.g. period-multiple orbits, quasi-periodic orbits and chaos [13, 17, 18, 19]. Nevertheless, several authors have characterised SMA elements in terms of the complex modulus (storage and loss modulus), which is usually used for elastomers to quantify their equivalent linear damping characteristics. Due to the SMA nonlinearities, the complex modulus is a function of the vibration amplitude and frequency, the level of pre-tension, the environmental temperature and the convective conditions [15, 20, 21, 22, 23]. On the other hand, Krack and Böttcher [24] proposed a method involving nonlinear modes to analyse dynamic systems with SMAs in the frequency domain, and highlighted that the complex modulus approach is not applicable in the case of rich dynamics.

A major drawback of using SMAs for control purposes is their limited bandwidth because fast heating and especially cooling of the elements require high level of thermal energy generation and transfer. For this reason control using SMAs usually involves passive adaptive approaches [7, 18]. For example, Williams et al. [25] proposed a PI controller, whose control objective is based on the relative phase between the primary and secondary masses for an adaptive tuned vibration absorber.

In this context the main contribution of this work lies in the integration of pseudoelastic SMA helical springs into a weakly nonlinear multibody dynamic system. A rigid rotor interacts with two passive magnetic bearings, whose housings are flexibly supported. Both the mechanical hysteresis and temperature depen-

dent stiffness properties of the SMA springs are explored aiming at reducing rotor lateral vibrations. The theoretical investigation is based on a multi-physics model linking constitutive relations of SMAs, weakly nonlinear passive magnetic bearing forces and the system dynamics. The results are compared to experiments carried out at a dedicated test-rig. A benchmark configuration of the test-rig with steel springs instead of SMA springs is used for comparison. The strong interplay between theoretical prediction and experimental observations is rare in this field [7, 8]. The investigations take into account and reflect on the main disadvantage using SMAs in relation to control, i.e. slow temperature changes. It is necessary to make abrupt stiffness changes in order to "jump" across critical speeds [3]. Alternatives are provided.

The paper is organized as follows. First the rotor-bearing test-rig is presented (Section 2) providing an overview of the system components. Modelling of the steel and SMA helical springs is presented in Section 3, including a short description of the constitutive model used and its interaction with the global spring behaviour. Also the complex modulus and the spring attachment system are treated. The weakly nonlinear passive magnetic bearings are described in Section 4. Section 5 concerns the multibody model, the equations of motion and their solution to describe the system dynamics. Experimental and theoretical results are presented in Section 6 followed by conclusions in Section 7.

2. Experimental set-up

The rotor-bearing system used in this investigation is shown in Fig. 1. The system stands out in the sense that it is designed to have a flexible rotor-bearing housing interaction, which allows interesting dynamic behaviour. The flexible interaction is provided by passive magnetic bearings with the advantage of having very low friction. The level of damping is low, and therefore sources of damping are required. The system consists of a vertical rigid shaft (⌀16×280 mm) and a disc on top with adjustable mass imbalance. The bottom of the shaft is connected to a DC motor through a flexible coupling that allows the rotor (shaft and disc) to tilt around the X and Y axes constituting two degrees of freedom. The coupling connection is shown in Fig. 1b.

Two passive magnetic bearings support the shaft. The magnetic fields in both bearings are generated by 20 ⌀10×20 mm cylinder neodymium magnets with vertical magnetization placed in a circular pattern. One similar magnet is located inside the shaft adjacent to each bearing. The bearings are repulsive in the lateral (horizontal) directions, which means that they are stable in the lateral direction and unstable in the axial direction. The coupling at bottom of the rotor is rigid in the axial direction, which means that the rotor-bearing coupling system is stable overall. All components are made from non-magnetizable materials (aluminium, brass, perspex) to avoid interfering with the magnetic fields. The bearing housings are supported by flexible steel beams resulting in two additional degrees of freedom. The lower bearing housing is able to move in the X direction, whereas the upper bearing is able to move in the Y direction relative to the lower bearing. The shaft rotation is measured using an encoder (HEDS-9140#A00 and HEDS-5140#A13 from Avago Technologies), the rotor tilt is measured using two proximitor sensors (TQ401 from Meggitt) located near the bottom of the shaft, and the horizontal motion of the upper bearing is measured by two accelerometers (type 4384 from Brüel & Kjær).

Helical springs, made from either steel or SMA, can be attached at the upper bearing housing, cf. Fig. 1, in the positive and negative X and Y directions (a total of four). The other ends of the springs are attached in a mechanism allowing different spring pre-tension lengths. Heat chambers can surround the springs. Two modified heat guns feed the heat chambers with hot air. A feedback control loop ensures a constant air temperature within ±0.3 °C. The electric power to the heat elements in the heat guns can be controlled and the air temperature of the heat chambers are measured using type T thermocouples. Control of air temperature and rotor velocity as well as data acquisition are carried out using a DS1103 dSpace board connected to a computer.

3. Helical springs

Two different types of springs can be inserted in the test-rig. The first type is made from an SMA, namely a pseudoelastic Nickel-Titanium alloy (Ni-Ti ratio of 56:44). In the following two sections the SMA

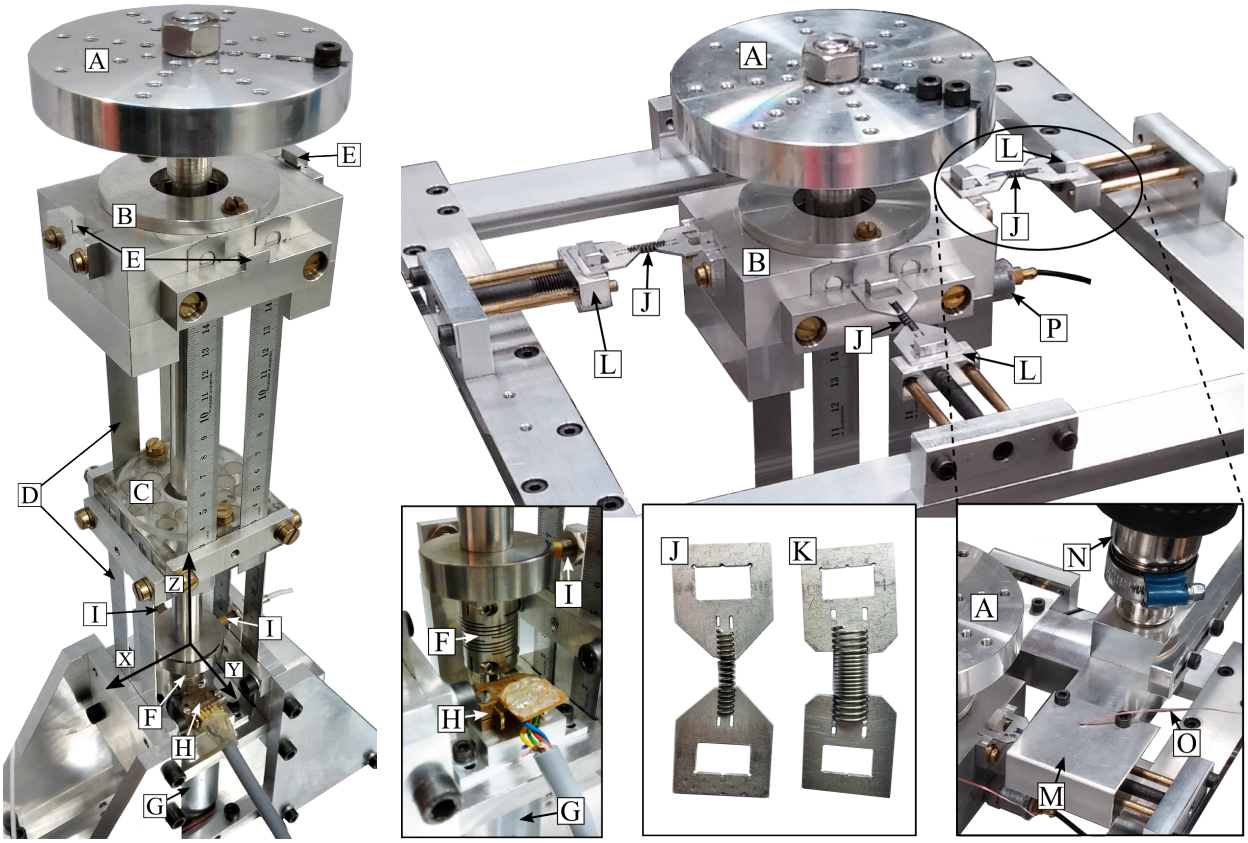

(a) (b)

Figure 1: Test-rig: (a) fundamental part and (b) spring attachment system and details. (A) Disc on top of shaft; (B) upper and (C) lower passive magnetic bearings supported by (D) flexible beams; (E) SMA spring attachment point at the upper bearing; at the bottom of the shaft is attached a (F) flexible coupling and then a (G) DC motor. An (H) encoder measures the rotor rotation and (I) proximity sensors measure the rotor tilt angles. (J) SMA and (K) steel springs attached in (L) variable pre-tension mechanism. A (M) heat chamber can surround the springs fed with hot air from a (N) heat gun. The temperature is measured using (O) thermocouples. (P) Accelerometers measure the upper bearing motion. The global coordinate system XYZ is also highlighted. Upper part of test-rig highlighting the spring attachment system.

constitutive model and the helical spring model are briefly outlined. Detailed descriptions and material parameters can be found in [23].

The second type of spring is made from spring steel (DIN 17223 C-wire) and it has a linear force-deflection relationship:

$$F_{\mathrm{t}} = -K_{\mathrm{t}} u - F_{\mathrm{t0}} \tag{1}$$

where K_{t} is the stiffness, u is the deflection and F_{t0} is a pre-tension force at the initial state, where the spring coils are in contact. The stiffness and pre-tension force have been determined experimentally by tensile tests. The steel springs are used for constituting a benchmark configuration of the rotor-bearing system to which the SMA configuration is compared. The basic properties of the two springs are listed in Tab. 1.

3.1. SMA constitutive model

The unusual properties of pseudoelastic SMAs are based on solid-state transformations between austenitic and martensitic crystallographic phases. The transformations can be induced by changes in either temperature (in the order of 10 °C) or stress (in the order of 100 MPa). The transformations result in significant

Table 1: Basic properties of helical springs.

Spring	SMA	Steel
Wire diameter, $2c$ (mm)	0.56	0.75
Spring diameter, $2r_0$ (mm)	2.56	6.25
Initial length, h_0 (mm)	6	10
Pre-tensioned length, h_p (mm)	12	16
Number of windings, n	6	12
Stiffness, K (N mm^{-1})	0.7 to 1.3	1.1
Initial force, F_0 (N)	0	3

strains (in the order of 5 %) and mechanical hysteresis. The large transformation strains cause considerable changes in tangential stiffness. The mechanical hysteresis can be used for damping purposes. The transformations are exo- and endothermic processes resulting in self-heating and cooling mechanisms and because SMAs have a tight thermo-mechanical coupling, also the strain rate becomes relevant.

A modified version of the constitutive modelling framework by Lagoudas et. al [26] is used to describe the thermo-mechanical behaviour of the SMA. The modified version is presented in [23]. The spring behaviour is primarily governed by a plane stress field having one normal component and a shear component, and therefore a model reduction to two dimensions is used. The governing equations are

$$\boldsymbol{\varepsilon} = \mathbf{S}\boldsymbol{\sigma} + \boldsymbol{\varepsilon}_\mathrm{t} \qquad\qquad \dot{\boldsymbol{\varepsilon}}_\mathrm{t} = \boldsymbol{\Lambda}\dot{\xi} \tag{2}$$

Here $\boldsymbol{\varepsilon} = \{\varepsilon_{11}, \gamma_{12}\}^\intercal$ is the strain vector, $\boldsymbol{\varepsilon}_\mathrm{t}$ is the phase transformation strain, $\boldsymbol{\sigma} = \{\sigma_{11}, \tau_{12}\}^\intercal$ is the stress vector, ξ is the martensitic phase fraction fulfilling $0 \leq \xi \leq 1$, $\mathbf{S}$ is the compliance tensor and it depends on elastic moduli of austenite and martensite, Poisson's ratio and the current value of the phase fraction, and $\boldsymbol{\Lambda}$ is the transformation direction tensor, and it is a function of the stress state and the direction of transformation.

Two transformation functions, Φ_f and Φ_r, are defined. They depend on the stress state $\boldsymbol{\sigma}$, the material temperature T, and the martensitic phase fraction ξ through the composite functions $f_\mathrm{f}(\zeta_\mathrm{f}(\xi, \xi_0))$ and $f_\mathrm{r}(\zeta_\mathrm{r}(\xi, \xi_0))$ respectively. Together with the constraints (i.e. Kuhn-Tucker conditions)

$$\dot{\xi} \geq 0, \quad \Phi_\mathrm{f}(\boldsymbol{\sigma}, T, \xi) \leq 0, \quad \Phi_\mathrm{f}\dot{\xi} = 0 \tag{3a}$$

$$\dot{\xi} \leq 0, \quad \Phi_\mathrm{r}(\boldsymbol{\sigma}, T, \xi) \leq 0, \quad \Phi_\mathrm{r}\dot{\xi} = 0 \tag{3b}$$

the transformation functions control whether or not forward (subscript f) or reverse (subscript r) transformations take place. The functions f_f and f_r are hardening functions that control the evolution of the martensitic phase fraction. They are designated by Bézier curves with curvature controlling parameters. The functions ζ_f and ζ_r are sub-loop functions, and they ensure smooth behaviour when phase transformations are incomplete and change direction at an intermediate state ($0 < \xi < 1$). The sub-loop functions have a curvature controlling parameter that controls the size of the hysteresis and the tangential stiffness during sub-looping. The hardening and sub-loop functions are modifications to the original model, and they are described in detail in [23].

The constitutive equations are coupled to the energy equation to take into account the latent heat of the phase transformations so that the SMA temperature may be different from the environmental conditions. Therefore the temperature becomes a dependent variable. The energy equation reads [23]:

$$\rho c_\mathrm{p}\dot{T} + \chi\dot{\xi} + \hat{h}\frac{2}{c}(T - T_\infty) = 0 \tag{4}$$

where $\chi = \chi(\boldsymbol{\sigma}, \xi)$ is a function closely related to the transformation functions. Here ρc_p is the volume specific heat capacity, $\hat{h}$ is the convection coefficient, c is the spring wire radius and T_∞ is the environmental temperature. The spring temperature is assumed uniform, and conduction through the spring ends to the grips is neglected.

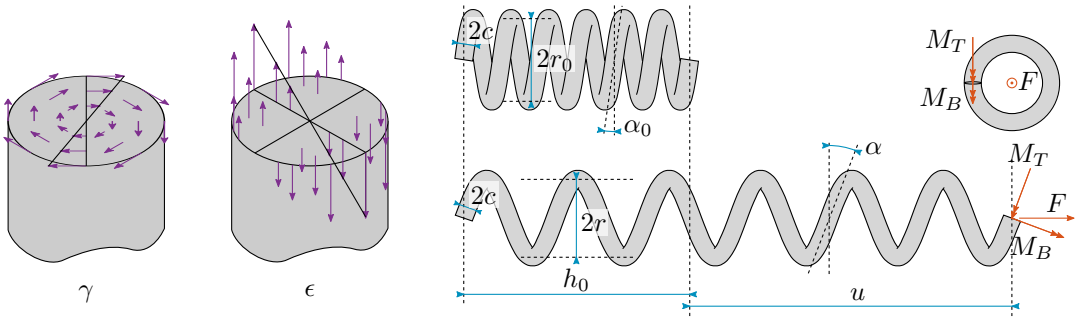

Figure 2: Illutration of shear and normal stress distribution in the wire cross section of a helical spring, together with characteristic properties of the spring in initial and loaded conditions.

The model has a number of parameters related to the specific material. The values of the parameters are provided in [23] and they are based on model calibration to experimental force-deflection tests. The convection coefficient $\hat{h}$ may have changed from the calibration value, because the environmental conditions related to the forced convection are slightly different in this work. However the theoretical results do not change significantly if the relative error is in the order of ± 10 %. The SMA springs have an initial training period, in which their thermo-mechanical properties change. Different training approaches may lead to quantitatively (but not qualitatively) different behaviour. This aspect is therefore a relevant source of error.

3.2. Helical spring model

Because of the large transformation strains it is possible to deform the SMA springs considerably resulting in large pitch angles of the coils. This means that geometrical nonlinearities are introduced. In these conditions both shear and normal strains are relevant, and the maximum components in the wire cross sections are [27]:

$$\varepsilon_{11}(c) = \frac{c}{r_0}\cos(\alpha_0)\left(\cos(\alpha_0) - \cos(\alpha)\right) \qquad \gamma_{12}(c) = \frac{c}{r_0}\cos(\alpha_0)\left(\sin(\alpha) - \sin(\alpha_0)\right) \tag{5}$$

The strain distributions and the spring itself are illustrated in Fig. 2. Here r_0 is the initial spring radius, c is the wire radius and α_0 and α are the initial and current pitch angles respectively. The initial angle is $\alpha_0 = \arctan\left(\frac{h_0}{2\pi n r_0}\right)$, where h_0 is the initial spring length and n is the number of windings. The current pitch angle is $\alpha = \arcsin\left(\frac{u}{L} + \sin\alpha_0\right)$, where $L = \sqrt{(2\pi n r_0)^2 + h_0^2}$ is the constant wire length and u is the axial deformation of the spring.

Because the strain distribution in the wire cross section is non-uniform and because of the material nonlinearities, the two dimensional cross sectional stress distribution becomes complex. The stress distribution is used for calculating the contributing bending and shear moments. However, the martensitic volume fraction can be considered constant throughout the wire cross section from a modelling point of view [23]. The result is a simple relation between a representative stress measure and the bending and shear moments:

$$M_\mathrm{B} = \frac{4}{3}c^3\sigma_{11}^* \qquad M_\mathrm{T} = \frac{2}{3}\pi c^3\tau_{12}^* \tag{6}$$

The representative stress $\boldsymbol{\sigma}^* = \{\sigma_{11}^*, \tau_{12}^*\}$ is found from the constitutive equations using the appertaining representative strain $\boldsymbol{\varepsilon}^* = \{\varepsilon_{11}^*, \gamma_{12}^*\}^\intercal = \{\frac{3\pi}{16}\varepsilon_{11}(c), \frac{3}{4}\gamma_{12}(c)\}^\intercal$. The resulting axial spring force is

$$F = \frac{\cos(\alpha_0)}{r_0}(M_T + M_B\tan(\alpha)) = \frac{2}{3}\frac{c^3}{r_0}\cos(\alpha_0)(\pi\tau_{12}^* + 2\sigma_{11}^*\tan(\alpha)) \tag{7}$$

The reader is referred to [11, 23] for an insight into the force-deflection relationship of SMA springs at different environmental temperatures.

3.3. Complex modulus

The intricate force-deflection relationship of the SMA springs can be quantified in terms of the complex modulus, which consists of the storage modulus (a measure of average stiffness) and the loss modulus (a measure of dissipated energy). The complex modulus is widely used in the fields of elastomers and hysteretic elements in general [28]. The advantage of using the complex modulus is that the relatively complicated SMA behaviour can be simplified into a single quantity having a real and an imaginary part that may be functions of e.g. vibration amplitude, frequency and ambient temperature. By using the complex modulus it significantly ease solution of the equations of motion in the time and frequency domains. The drawback is that some dynamic content may be lost. This is especially relevant if the response is assumed to be simple harmonic as it is in this case. However, it should be emphasised that if the complex modulus is a function of the vibration amplitude and frequency and the ambient temperature, it is still possible to explore weak nonlinearities.

To use the complex modulus the dynamic problem has to be converted to involve complex states. The actual deflection response $u(t)$ that the SMA spring is subjected to is therefore written as $u(t) = \Re\{z(t)\} + u_0$, where $z(t)$ is a complex state, and u_0 is the static equilibrium. The complex SMA force is then

$$F_z(t) = -K_\mathrm{s} z(t) - F_\mathrm{s0} \tag{8}$$

Here $K_\mathrm{s} = k_\mathrm{s}(1 + \mathrm{i}\eta)$ is the complex modulus[1], where k_s is the storage modulus, η is the loss factor, i is the imaginary unit, and $F_\mathrm{s0} = F_\mathrm{s0}(u_0)$ is the static (and real) force at the equilibrium. The actual SMA spring force is $F_\mathrm{s}(t) = \Re\{F_z(t)\}$. In the case of a simple harmonic response, i.e.

$$u(t) = \frac{1}{2}\left(Z\,\mathrm{e}^{\mathrm{i}\omega t} + \bar{Z}\,\mathrm{e}^{-\mathrm{i}\omega t}\right) + u_0 = A\cos(\omega t + \phi) + u_0 \tag{9}$$

we get

$$F_s(t) = -\frac{1}{2}\left(K_\mathrm{s} Z\,\mathrm{e}^{\mathrm{i}\omega t} + \bar{K}_\mathrm{s}\bar{Z}\,\mathrm{e}^{-\mathrm{i}\omega t}\right) - F_\mathrm{s0} = -k_s\sqrt{1+\eta^2}A\cos(\omega t + \phi + \arctan(\eta)) - F_\mathrm{s0} \tag{10}$$

where ω is the frequency, $A = |Z|$ and $\phi = \arg Z$ are the response amplitude and phase respectively. The complex modulus can be determined either experimentally or by the use of the SMA spring model described in the former sections. In both cases, the storage modulus and the loss factor are

$$k_s = \frac{\oint F_s\,\mathrm{d}\,v}{\pi A^2} \qquad\qquad \eta = \frac{\oint F_s\,\mathrm{d}\,u}{\oint F_s\,\mathrm{d}\,v} \tag{11}$$

where $v(t) = \Im\{z(t)\} = \frac{1}{2\mathrm{i}}\left(Z\,\mathrm{e}^{\mathrm{i}\omega t} - \bar{Z}\,\mathrm{e}^{-\mathrm{i}\omega t}\right) = A\sin(\omega t + \phi)$. In this context the complex modulus and the pre-tension force are functions of the response amplitude A, the frequency ω and the environmental temperature T.

The storage modulus k_s, the loss factor η and the pre-tension force F_s0 calculated using the SMA spring model may be seen in Fig. 3. All three quantities strongly depend on the ambient temperature, and k_s and F_s0 increase with temperature whereas η decreases. From 30 °C to 70 °C there is close to a factor of two in difference for all three quantities. The dependencies on frequency are weaker but similar: k_s and F_s0 increase with frequency whereas η decreases. It should be noticed that at very low frequencies (below approximately 0.5 Hz) the behaviour is more complicated [23]. The dependencies on deflection amplitude are also weak compared to the temperature dependencies and they are non-monotonic. For example η has optimal conditions in terms of amplitude. We emphasize that the SMA model has been calibrated using data with deflection amplitudes larger than 2 mm and frequencies lower than 10 Hz. This means that the behaviour having amplitudes below 2 mm or frequencies above 10 Hz are more uncertain and relies on the overall model validity.

[1] In this context the complex modulus is measured in N m^{-1}, thus being a complex stiffness.

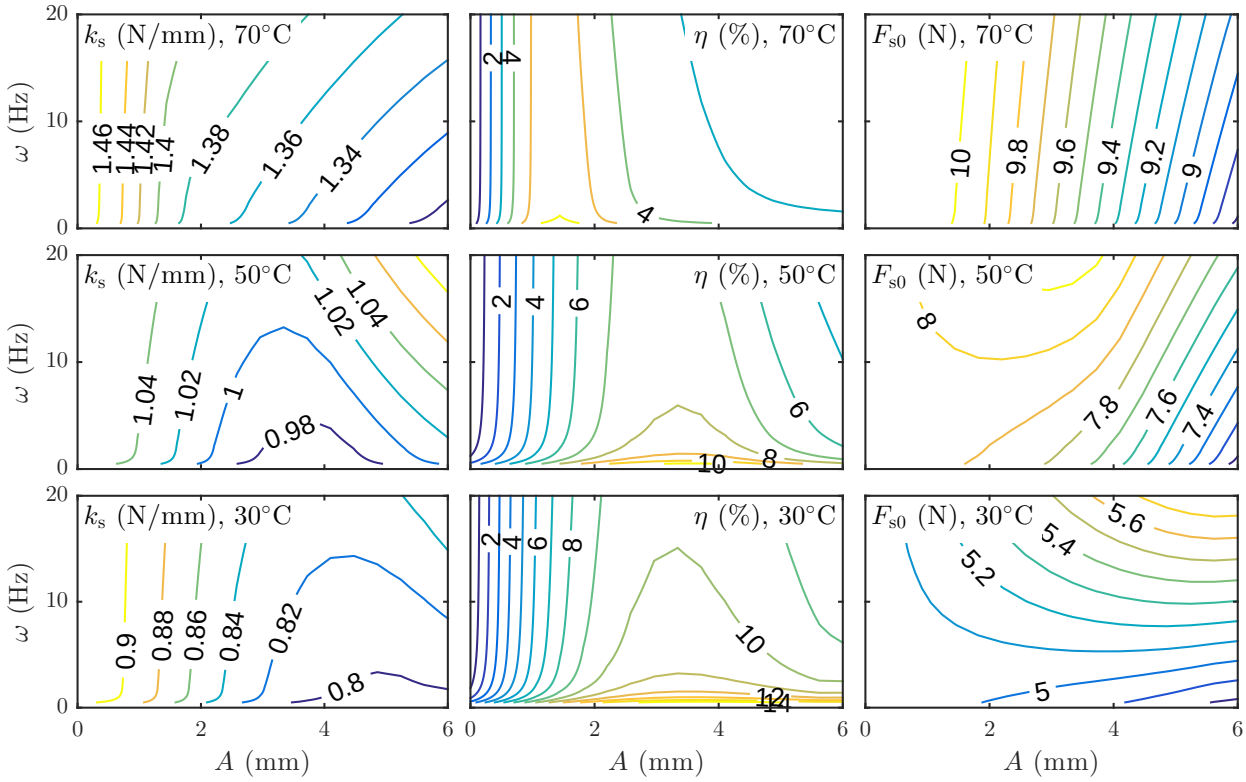

Figure 3: Complex modulus and pre-tension force of SMA spring depending on deflection amplitude A and frequency ω and ambient temperature T. The pre-tension length $u_0 = 6$ mm is constant. The values are calculated using the spring model.

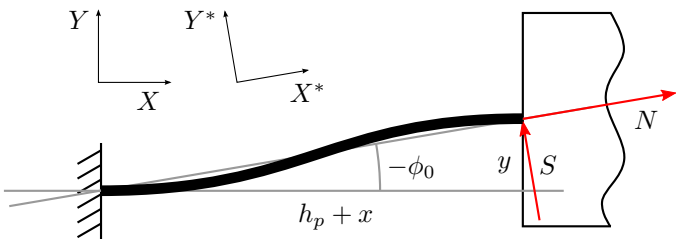

Figure 4: Illustration of clamping conditions for the springs exemplified with the spring attached at $(-h_\mathrm{p}, 0)$. To the left is the fixture, to the right the upper bearing.

3.4. Spring attachment

To the upper bearing housing there are attached four springs of either steel or SMA. They are attached at the $-X$, $-Y$, X and Y faces of the bearing housing. The lengths of the springs are identical and equal to h_p (cf. Tab. 1) at the equilibrium of the system.

The ends of the helical springs (both steel and SMA) are subjected to conditions similar to clamping of a beam, which becomes significant when deflections are lateral to the spring axis. The lateral characteristics of a spring can be approximated using equivalent properties to a beam, namely the axial, flexural and shear rigidities [27]:

$$(EA)_\mathrm{spring} = \frac{Gc^4h}{4nr^3} \approx N \qquad (EI)_\mathrm{spring} = \frac{2hEIG}{\pi nr(2G+E)} \approx 1.1Nr^2 \qquad (\kappa AG)_\mathrm{spring} = \frac{hEI}{\pi nr^3} \approx 2.6N \tag{12}$$

where N is the axial tensile force of the spring at the current state, $I = \frac{\pi}{4}c^4$ is the second area moment of inertia, $E = 2G(1+\nu)$ is the elastic modulus and $\nu \approx 0.3$ is Poisson's ratio. It should be noted that the equations provided in [27] hold the assumptions that the coil pitch angle is small and that the material is linearly elastic.

Having these properties, the helical spring is approximated to behave as a quasi-static Timoshenko beam subjected to an axial tensile load [29]:

$$\kappa AG\,(w'' - \phi') + Nw'' = 0 \tag{13}$$

$$EI\phi'' + \kappa AG\,(w' - \phi) = 0 \tag{14}$$

Here w is the deflection, ϕ is the bending angle and the moment and shear force resultants are $M = -EI\phi'$ and $Q = \kappa AG\,(w' - \phi) + Nw'$ respectively. A coordinate system X^*Y^* is set up as indicated in Fig. 4, and it follows the movement of the spring end that is attached to the upper bearing housing having the coordinates (x, y) in the XY reference. In the X^*Y^* reference the equivalent beam is subjected to the following boundary conditions $w(0) = w(h) = 0$ and $\phi(0) = \phi(h) = -\phi_0$, where $h = \sqrt{(h_\mathrm{p}+x)^2 + y^2}$ is the deformed length of the spring. The solution to the beam equations gives the following relation between the angle ϕ_0 and the resultant shear force at the beam ends $S = Q(0) = Q(h)$:

$$\phi_0 = S\left(\frac{hc_2}{2\kappa AGc_1}\frac{\mathrm{e}^{c_1c_2h}+1}{\mathrm{e}^{c_1c_2h}-1} - \frac{1}{N}\right) \tag{15}$$

where $c_1^2 = \frac{N}{N+\kappa AG}$ and $c_2^2 = \frac{\kappa AG}{EI}$. The approximative equivalent spring properties, Eq. (12), are inserted into Eq. (15), and the resulting shear force is

$$S \approx \phi_0 N c_\mathrm{s}\,, \quad c_\mathrm{s}^{-1} = \frac{0.55h}{r}\frac{\mathrm{e}^{0.80h/r}+1}{\mathrm{e}^{0.80h/r}-1} - 1 \tag{16}$$

The spring attached at $(-h_\mathrm{p}, 0)$ has the angle $\phi_0 = \arctan\left(\frac{y}{h_\mathrm{p}+x}\right)$. The tensile force is found using Eq. (1) for the steel spring and Eq. (7) for the SMA spring. It is assumed that the clamping of the SMA spring

does not influence the axial force determined by Eq. (7). The forces acting on the bearing housing from the spring attached at $(-h_\mathrm{p}, 0)$ are

$$F_{x,1} = -\left(N\cos(\phi_0) - S\sin(\phi_0)\right) \qquad F_{y,1} = -\left(N\sin(\phi_0) + S\cos(\phi_0)\right) \tag{17}$$

The procedure is similar for the other three springs. The axial spring force N is equal to $-F_\mathrm{t}$ from Eq. (1) (steel spring) or $-F_\mathrm{s}$ from Eq. (7) (SMA spring). The forces are in both cases evaluated for the deflection $u = h - h_0$.

Approximations of the summed forces from the four springs using small angles $\phi_0 \ll 1$ are

$$F_x = \sum_{i=1}^{4} F_{x,i} = -2\left[K + \frac{F_0}{h_\mathrm{p}}(1 + c_\mathrm{s})\right]x \qquad F_y = \sum_{i=1}^{4} F_{y,i} = -2\left[K + \frac{F_0}{h_\mathrm{p}}(1 + c_\mathrm{s})\right]y \tag{18}$$

because $N = Kx + F_0$. Here c_s is evaluated at $h = h_\mathrm{p}$, F_0 is the spring force and K is the stiffness evaluated at a deflection of h_p. From these equations it is evident that the pre-tension force has a significant impact on the provided stiffness because K and $\frac{F_0}{h_\mathrm{p}}$ are of the same order of magnitude. Note that the term $\frac{F_0}{h_\mathrm{p}}$ in F_x comes from the springs attached in the Y direction and not in the X direction. The steel springs has $c_\mathrm{s} = 0.52$ and the SMA springs has $c_\mathrm{s} = 0.24$ evaluated at $h = h_\mathrm{p}$, and because these numbers are of the order 1 it means that the addition of the clamping is significant.

4. Magnetic shaft-bearing interaction

The model for the magnetic interaction between the shaft and the bearings is thoroughly described in [30], in which weak nonlinearities of the magnetic interaction are investigated for the same test-rig without steel and SMA springs attached. The model is based on calculation of the magnetic flux density produced by each bearing magnet. The flux densities are super-positioned, and the force from the collected bearing flux density on the shaft magnet is calculated at different shaft positions. The magnetic forces were approximated using a Taylor series expansion with high accuracy. A maximum residual standard deviation less than 0.2 percent relative to the full scale force was achieved. The approximation is

$$F_\mathrm{m} = \begin{Bmatrix} -k_\mathrm{m}x_\mathrm{r} - \kappa x(x_\mathrm{r}^2 + y_\mathrm{r}^2) \\ -k_\mathrm{m}y_\mathrm{r} - \kappa y(x_\mathrm{r}^2 + y_\mathrm{r}^2) \\ f_z \end{Bmatrix} \tag{19}$$

where $(x_\mathrm{r}, y_\mathrm{r})$ is the relative horizontal coordinates between the shaft magnet and the bearing centre, k_m is the linear lateral stiffness, κ is the cubic lateral stiffness and f_z is a constant force due to a vertical (axial) misalignment z_0 between the bearing centre and the shaft magnet as a consequence of manufacturing inaccuracies. Because $\kappa > 0$ the bearings exhibit a stiffening effect.

Because of imperfections in the magnets, the bearing magnets exhibit significant non-uniformity. This means that the forces between the bearings and shaft depend on the rotation angle of the shaft. It also affects the equilibrium position. However, it was shown in [30] that the magnetic non-uniformity together with geometrical inaccuracies of the shaft can be collected into an equivalent eccentricity having an amplitude and a phase. This means that the relative coordinate between the magnetic centre of the shaft and a bearing is

$$x_\mathrm{r} = x_\mathrm{s} + e\cos(\theta + \phi) - x \qquad y_\mathrm{r} = y_\mathrm{s} + e\sin(\theta + \phi) - y \tag{20}$$

where $(x_\mathrm{s}, y_\mathrm{s})$ is the horizontal coordinate of the shaft, (x, y) is the horizontal coordinate of the bearing, and (e, ϕ) is the amplitude and phase of the collected magnetic and geometrical non-uniformity. The lower bearing has the eccentricity (e_1, ϕ_1), the upper bearing (e_2, ϕ_2). The eccentricities result in harmonic and nonlinear parametric excitation of the system.

The heat chambers used for the SMA springs are next to the upper bearing. This means that hot air warms up both the bearing magnets and the appertaining shaft magnet. According to the supplier of

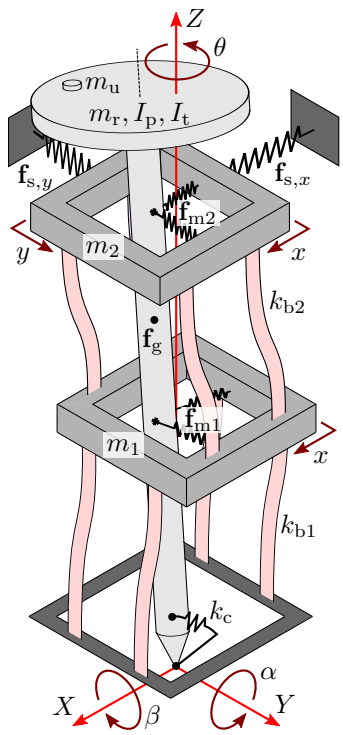

Figure 5: Schematic of dynamic system, consisting of the shaft and disc or rotor (light grey), two bearing housings (grey) and eight flexible beams (light red).

the magnets (Sintex a/s), the remanence (remaining magnetic flux density) of the magnets have a relative temperature sensitivity of $-0.11\ \%\ \mathrm{K}^{-1}$. The remanence is proportional to the magnetization of the magnets, and the magnetic forces are proportional to the square of the magnetization [30, 31]. This means that the magnetic forces (and stiffnesses) of the upper bearing are reduced by approximately 1 %, 5 % and 10 % when operating at 30 °C, 50 °C and 70 °C respectively compared to the calibration temperature of 25 °C.

5. Modelling the dynamics

A schematic of the mechanical system is shown in Fig. 5. The rotor-bearing system has four degrees of freedom: α, β, x and y. The two first degrees of freedom (α, β) denote the tilting angles of the shaft around the Y and $-X$ axes respectively. This means that a positive value of α corresponds to a displacement of the tip of the shaft in the direction of positive X, and similar for β in relation to Y. The rotational angle of the shaft is denoted θ, and $\dot{\theta} = \omega$ is the angular velocity controlled by the DC motor in the lower end of the shaft. The polar inertia I_p of the shaft and disc results in gyroscopic forces. The shaft is supported by a flexible coupling at its bottom. The coupling is flexible in bending (α and β), and it is stiff in torsion (θ) and in its axial direction (Z). For this reason the coupling is modelled to provide a linear angular stiffness k_c at the shaft pivot point, and it constrains torsional and axial movement of the shaft. The shaft and disc is affected in the $-Y$ direction by the gravitational force $\mathbf{f}_\mathrm{g}$ with magnitude $m_\mathrm{r} g$ at the centre of mass, located at the vertical distance l_g from the pivot point. The rotor mass is m_r and g is the gravitational constant. Imbalance (residual and added) influences the shaft tilt, and it is modelled as a reaction force from a point mass m_u, with the axial distance l_u and radial distance r_u from the pivot point, and the point mass is subjected to a radial acceleration of $r_\mathrm{u}\omega^2$. The magnetic forces from the lower and upper bearings ($\mathbf{f}_{\mathrm{m1}}$ and $\mathbf{f}_{\mathrm{m2}}$ in Fig. 5) as described in the Section 4 act on the shaft in the axial positions l_1 and l_2 from the pivot point respectively.

The bearing housings are supported by flexible steel beams that are modelled to provide forces with linear stiffness in one horizontal direction each. In the other horizontal direction, the beams are stiff, so they constrain the bearing housing from moving. Therefore, the two last degrees of freedom, (x, y), denote the displacement in the XY plane of the upper bearing housing. The lower bearing housing follows synchronously the upper bearing housing in the X direction, but it is constrained in the Y direction. For this reason the lower bearing housing has the horizontal coordinates $(x, 0)$. The beams connecting the fixed support and the lower bearing housing have the collected horizontal stiffness $k_{\mathrm{b}1}$, and $k_{\mathrm{b}2}$ is the similar stiffness of the beams connecting the two bearing housings. The magnetic forces acting on the bearings are opposite of the ones acting on the shaft by Newton's third law. The steel or SMA spring forces act on the upper bearing housing in the X and Y direction ($\mathbf{f}_{\mathrm{s},x}$ and $\mathbf{f}_{\mathrm{s},y}$ in Fig. 5) as described in Section 3.4.

The equations of motions are established using Newton's second law for the bearing housings and Euler's equation about the pivot point for the collected shaft and disc (rotor). A detailed description is provided in [30]. Assuming that $\alpha, \beta \ll 1$ the equations of motion are

$$\mathbf{M}\ddot{\mathbf{x}} + (\mathbf{C} + \omega\mathbf{G})\dot{\mathbf{x}} + \mathbf{K}\mathbf{x} = \mathbf{f}_{\mathrm{l}} + \mathbf{f}_{\mathrm{nl}} + \mathbf{f}_{\mathrm{s}} \tag{21}$$

where $\mathbf{x} = \{\alpha, \beta, x, y\}^{\intercal}$ is the state vector, $\mathbf{M}$ is the mass matrix, $\mathbf{C} = c_{\mathrm{m}}\mathbf{M} + c_{\mathrm{k}}\mathbf{K}$ is the mass and stiffness proportional structural damping matrix, $\mathbf{G}$ is the gyroscopic matrix, and $\mathbf{K}$ is the stiffness matrix. The matrices are

$$\begin{aligned}
\mathbf{M} &= \begin{bmatrix} I_{\mathrm{t}} & 0 & 0 & 0 \\ 0 & I_{\mathrm{t}} & 0 & 0 \\ 0 & 0 & m_1 + m_2 & 0 \\ 0 & 0 & 0 & m_2 \end{bmatrix} \qquad \mathbf{G} = \begin{bmatrix} 0 & I_{\mathrm{p}} & 0 & 0 \\ -I_{\mathrm{p}} & 0 & 0 & 0 \\ 0 & 0 & 0 & 0 \\ 0 & 0 & 0 & 0 \end{bmatrix} \\
\mathbf{K} &= \begin{bmatrix} k_K & 0 & -k_1 l_1 - k_2 l_2 & 0 \\ 0 & k_K & 0 & -k_2 l_2 \\ -k_1 l_1 - k_2 l_2 & 0 & k_{b1} + k_1 + k_2 & 0 \\ 0 & -k_2 l_2 & 0 & k_{b2} + k_2 \end{bmatrix}
\end{aligned} \tag{22}$$

where I_{t} is the transversal inertia of the rotor, m_1 and m_2 are masses of the lower and upper bearing houses respectively and $k_K = k_c - l_{\mathrm{g}} m_{\mathrm{r}} g + f_{z1} l_1 + f_{z2} l_2 + k_1 l_1^2 + k_2 l_2^2$. The magnetic stiffnesses and misalignment forces of the lower and upper bearings are k_1, f_{z1} and k_2, f_{z2} respectively, cf. Section 4. At the right hand side of Eq. (21) are linear excitation forces $\mathbf{f}_{\mathrm{l}}$, nonlinear magnetic forces $\mathbf{f}_{\mathrm{nl}}$, and spring force $\mathbf{f}_{\mathrm{s}}$. The linear excitation forces are

$$\mathbf{f}_{\mathrm{l}} = \begin{Bmatrix} u\omega^2 \cos(\theta + \phi_{\mathrm{u}}) - (k_1 l_1 + f_{z1}) e_1 \cos(\theta + \phi_1) - (k_2 l_2 + f_{z2}) e_2 \cos(\theta + \phi_2) \\ u\omega^2 \sin(\theta + \phi_{\mathrm{u}}) - (k_1 l_1 + f_{z1}) e_1 \sin(\theta + \phi_1) - (k_2 l_2 + f_{z2}) e_2 \sin(\theta + \phi_2) \\ k_1 e_1 \cos(\theta + \phi_1) + k_2 e_2 \cos(\theta + \phi_2) \\ k_2 e_2 \sin(\theta + \phi_2) \end{Bmatrix} \tag{23}$$

where $u = m_{\mathrm{u}} r_{\mathrm{u}} l_{\mathrm{u}}$ is the amplitude of the imbalance moment and ϕ_{u} is its phase. If the rotational frequency is constant, then $\theta = \omega t$.

The vector of nonlinear forces comprises the most pronounced nonlinearities related to the cubic terms of the passive magnetic bearing forces:

$$\mathbf{f}_{\mathrm{nl}} = \begin{Bmatrix} -\kappa_1 l_1 x_{\mathrm{a}} \left(x_{\mathrm{a}}^2 + y_{\mathrm{a}}^2\right) - \kappa_2 l_2 x_{\mathrm{b}} \left(x_{\mathrm{b}}^2 + y_{\mathrm{b}}^2\right) \\ -\kappa_1 l_1 y_{\mathrm{a}} \left(x_{\mathrm{a}}^2 + y_{\mathrm{a}}^2\right) - \kappa_2 l_2 y_{\mathrm{b}} \left(x_{\mathrm{b}}^2 + y_{\mathrm{b}}^2\right) \\ \kappa_1 x_{\mathrm{a}} \left(x_{\mathrm{a}}^2 + y_{\mathrm{a}}^2\right) + \kappa_2 x_{\mathrm{b}} \left(x_{\mathrm{b}}^2 + y_{\mathrm{b}}^2\right) \\ \kappa_2 y_{\mathrm{b}} \left(x_{\mathrm{b}}^2 + y_{\mathrm{b}}^2\right) \end{Bmatrix} \tag{24}$$

where

$$x_{\mathrm{a}} = l_1 \alpha + e_1 \cos(\theta + \phi_1) - x \qquad y_{\mathrm{a}} = l_1 \beta + e_1 \sin(\theta + \phi_1) \tag{25}$$

$$x_{\mathrm{b}} = l_2 \alpha + e_2 \cos(\theta + \phi_2) - x \qquad y_{\mathrm{b}} = l_2 \beta + e_2 \sin(\theta + \phi_2) - y \tag{26}$$

Table 2: System parameters.

Property	Value	Property	Value	Property	Value
g (N kg^{-1})	9.81	m_r (kg)	0.616	f_{z1} (N)	-0.01
k_c (N m)	0.7	m_1 (kg)	0.474	f_{z2} (N)	-5.04
c_m (s^{-1})	0.57	m_2 (kg)	1.410	$k_{\mathrm{b}1}$ (N m^{-1})	$1.18 \cdot 10^3$
c_k (s)	$16 \cdot 10^{-3}$	I_t (kg m^2)	$31.2 \cdot 10^{-3}$	$k_{\mathrm{b}2}$ (N m^{-1})	$0.72 \cdot 10^3$
u (kg m^2)	$14.8 \cdot 10^{-6}$	I_p (kg m^2)	$326 \cdot 10^{-6}$	k_1 (N m^{-1})	$1.66 \cdot 10^3$
e_1 (m)	$0.11 \cdot 10^{-3}$	l_g (m)	0.188	k_2 (N m^{-1})	$1.61 \cdot 10^3$
e_2 (m)	$0.14 \cdot 10^{-3}$	l_1 (m)	0.118	κ_1 (N m^{-3})	$9.37 \cdot 10^6$
ϕ_u (°)	7	l_2 (m)	0.263	κ_2 (N m^{-3})	$6.78 \cdot 10^6$
ϕ_1 (°)	38				
ϕ_2 (°)	-118				

The collected spring force vector from the four springs is (cf. Eq. (17))

$$\mathbf{f}_\mathrm{s} = \sum_{i=1}^{4} \begin{Bmatrix} 0 & 0 & F_{x,i} & F_{y,i} \end{Bmatrix}^\mathsf{T} \tag{27}$$

The system parameters are provided in Tab. 2.

The proportional damping parameters c_m and c_k are determined such that the damping factor is 1 % at 7 Hz and 13 Hz. The result is $c_\mathrm{m} = 0.57$ s^{-1} and $c_\mathrm{k} = 16 \cdot 10^{-3}$ s. This is based on the transient responses (Section 6.1) and the ramp-ups (Section 6.2) such that the results obtained by simulation of the steel spring system configuration match the experimental results to a large extent. When calculating the damping matrix $\mathbf{C}$ that depends on the stiffness matrix $\mathbf{K}$, the stiffnesses of the steel springs, Eq. (18), are also included, because the springs and their attachment indeed contribute to the damping. The damping matrix is identical for the SMA system configuration.

The parameter values related to the eccentricities of the shaft magnets are identical to the ones obtained in [30]. We have added one imbalance mass on the disc having $(u_\mathrm{a}, \phi_\mathrm{a}) = (11.9 \text{ kg mm}^2, -10°)$. Together with the residual imbalance moment of $(u_\mathrm{r}, \phi_\mathrm{r}) = (4.9 \text{ kg mm}^2, 52°)$ obtained in [30] the resulting imbalance moment becomes $(u, \phi) = (14.8 \text{ kg mm}^2, 7°)$ by vector addition.

By transforming the equations of motion into first order ordinary differential equations, they are solved using the Runge-Kutta-Fehlberg algorithm, which is the adaptive version of the Runge-Kutta 45 method. The SMA temperature also evolve over time. However, this dependence is calculated internally in the SMA model using the implicit Euler method. The equations of motions are also solved in the frequency domain as described in the next section.

5.1. Solution in frequency domain

In order to determine the frequency response of the system, i.e. the steady state response for constant rotational frequency, it is convenient to solve the equations of motion in the frequency domain. It is far less computationally expensive compared to time domain solutions. However, the solution is only approximate because of several simplifying assumptions, which are explained below. The validity of the modelling approach, and therefore the assumptions, is justified in Section 6.3.

The only forcing frequency is the rotational frequency ω, cf. Eq. (23). It is assumed that the steady state system response is simple harmonic with the same frequency as the excitation:

$$\mathbf{x}(t) = \frac{1}{2}\left(\mathbf{z}\,\mathrm{e}^{\mathrm{i}\omega t} + \bar{\mathbf{z}}\,\mathrm{e}^{-\mathrm{i}\omega t}\right) \tag{28}$$

where $\mathbf{z} = \{z_\alpha, z_\beta, z_x, z_y\}^\mathsf{T}$ is the complex representation of the response amplitude and phase. This assumption is reasonable because a large extent of the system is linear and because the nonlinearities are weak. More specifically, the nonlinear contributions are the magnetic bearings forces (resulting in the cubic stiffness

κ), which also enter as parametric forcing, and the SMA spring forces, which enter through a mounting also introducing geometrical nonlinearities. Both contributions are only weakly nonlinear. The assumed solution is inserted into the equations of motion (21) and higher order harmonics are neglected resulting in

$$\frac{1}{2}\left(\mathbf{F}(\mathbf{z},\omega)\,\mathrm{e}^{\mathrm{i}\omega t} + \overline{\mathbf{F}(\mathbf{z},\omega)}\,\mathrm{e}^{-\mathrm{i}\omega t}\right) = \mathbf{0}\ , \tag{29}$$

$$\mathbf{F}(\mathbf{z},\omega) = \left(-\omega^2\mathbf{M} + \mathrm{i}\omega(\mathbf{C}+\omega\mathbf{G}) + \mathbf{K} + \mathbf{K}_\mathrm{s}(\mathbf{z},\omega)\right)\mathbf{z} - \mathbf{q}_\mathrm{l}(\omega) - \mathbf{q}_\mathrm{nl}(\mathbf{z}) \tag{30}$$

Equation (29) should be satisfied for all t, implying that $\mathbf{F}(\mathbf{z},\omega) = \mathbf{0}$. The linear external forcing term $\mathbf{q}_\mathrm{l}(\omega)$ becomes

$$\mathbf{q}_\mathrm{l}(\omega) = \begin{Bmatrix} \omega^2 z_\mathrm{u} - (k_1 l_1 + f_{z1})z_1 - (k_2 l_2 + f_{z2})z_2 \\ -\omega^2 \mathrm{i} z_\mathrm{u} + (k_1 l_1 + f_{z1})\mathrm{i} z_1 + (k_2 l_2 + f_{z2})\mathrm{i} z_2 \\ k_1 z_1 + k_2 z_2 \\ -k_2 \mathrm{i} z_2 \end{Bmatrix} \tag{31}$$

where $z_\mathrm{u} = u\,\mathrm{e}^{\mathrm{i}\phi_\mathrm{u}}$, $z_1 = e_1\,\mathrm{e}^{\mathrm{i}\phi_1}$ and $z_2 = e_2\,\mathrm{e}^{\mathrm{i}\phi_2}$. The nonlinear forces $\mathbf{q}_\mathrm{nl}(\mathbf{z})$ related to the magnetic bearings are

$$\mathbf{q}_\mathrm{nl}(\mathbf{z}) = \frac{1}{4}\begin{Bmatrix} -\kappa_1 l_1\left[2z_{x\mathrm{a}}|z_{y\mathrm{a}}|^2 + \bar{z}_{x\mathrm{a}}\left(3z_{x\mathrm{a}}^2 + z_{y\mathrm{a}}^2\right)\right] - \kappa_2 l_2\left[2z_{x\mathrm{b}}|z_{y\mathrm{b}}|^2 + \bar{z}_{x\mathrm{b}}\left(3z_{x\mathrm{b}}^2 + z_{y\mathrm{b}}^2\right)\right] \\ -\kappa_1 l_1\left[2z_{y\mathrm{a}}|z_{x\mathrm{a}}|^2 + \bar{z}_{y\mathrm{a}}\left(3z_{y\mathrm{a}}^2 + z_{x\mathrm{a}}^2\right)\right] - \kappa_2 l_2\left[2z_{y\mathrm{b}}|z_{x\mathrm{b}}|^2 + \bar{z}_{y\mathrm{b}}\left(3z_{y\mathrm{b}}^2 + z_{x\mathrm{b}}^2\right)\right] \\ \kappa_1\left[2z_{x\mathrm{a}}|z_{y\mathrm{a}}|^2 + \bar{z}_{x\mathrm{a}}\left(3z_{x\mathrm{a}}^2 + z_{y\mathrm{a}}^2\right)\right] + \kappa_2\left[2z_{x\mathrm{b}}|z_{y\mathrm{b}}|^2 + \bar{z}_{x\mathrm{b}}\left(3z_{x\mathrm{b}}^2 + z_{y\mathrm{b}}^2\right)\right] \\ \kappa_2\left[2z_{y\mathrm{b}}|z_{x\mathrm{b}}|^2 + \bar{z}_{y\mathrm{b}}\left(3z_{y\mathrm{b}}^2 + z_{x\mathrm{b}}^2\right)\right] \end{Bmatrix} \tag{32}$$

where $z_{x\mathrm{a}} = l_1 z_\alpha + z_1 - z_x$, $z_{y\mathrm{a}} = l_1 z_\beta - \mathrm{i}z_1$, $z_{x\mathrm{b}} = l_2 z_\alpha + z_2 - z_x$ and $z_{y\mathrm{b}} = l_2 z_\beta - \mathrm{i}z_2 - z_y$.

The forces from either the steel or SMA springs can be represented in the frequency domain with the use of the complex modulus as described in Section 3.3. A first order approximation of the fundamental harmonic content of the spring forces are provided in Eq. (18). Combined with the complex modulus, the total force $\mathbf{f}_\mathrm{s}$ becomes

$$\mathbf{f}_\mathrm{s} = -\frac{1}{2}\left(\mathbf{K}_\mathrm{s}(\mathbf{z},\omega)\mathbf{z}\,\mathrm{e}^{\mathrm{i}\omega t} + \bar{\mathbf{K}}_\mathrm{s}(\mathbf{z},\omega)\bar{\mathbf{z}}\,\mathrm{e}^{-\mathrm{i}\omega t}\right)\ , \tag{33}$$

$$\mathbf{K}_\mathrm{s}(\mathbf{z},\omega) = 2\begin{bmatrix} 0 & 0 & 0 & 0 \\ 0 & 0 & 0 & 0 \\ 0 & 0 & K_x + \frac{F_{0y}}{h_\mathrm{p}}(1+c_\mathrm{s}) & 0 \\ 0 & 0 & 0 & K_y + \frac{F_{0x}}{h_\mathrm{p}}(1+c_\mathrm{s}) \end{bmatrix} \tag{34}$$

For the steel springs we have that $K_x = K_y = K_\mathrm{t}$ and $F_{0x} = F_{0y} = F_{\mathrm{t}0} + K_\mathrm{t}(h_\mathrm{p} - h_0)$ related to Eq. (1) and Tab. 1. For the SMA springs, the complex stiffness and the pre-tension forces are functions of the pre-tension length (which is constant), the vibration amplitude of the upper bearing housing, the oscillation frequency and the ambient temperature, i.e. $K_x = K_\mathrm{s}(h_\mathrm{p} - h_0, |z_x|, \omega, T_\infty)$ and $F_{0x} = F_{\mathrm{s}0}(h_\mathrm{p} - h_0, |z_x|, \omega, T_\infty)$ and similar for the y components. Both K_s and $F_{\mathrm{s}0}$ are calculated a priori for a number of interpolation points, and during the solution in the frequency domain the functions are evaluated by linear interpolation between the points.

Notice that there are two different kinds of approximations related to $\mathbf{f}_\mathrm{s}$. The first is related to material nonlinearities of the SMAs, which are linearised using the complex modulus. However, F_0 and K_s are still functions of $\mathbf{z}$ and ω. The second kind is related to geometrical nonlinearities of the attachment of the springs, where (a) only the fundamental harmonic is taken into account, and (b) a first order approximation to the fundamental harmonic content is made. This is different from the nonlinear magnetic forces, for which the fundamental harmonic content is provided to the order three.

The system of complex equations $\mathbf{F}(\mathbf{z}, \omega) = \mathbf{0}$ is solved in an interval of frequencies using the method of pseudo-arclength continuation. The method is described in [32]. First, a solution is found at the lowest frequency of interest using a Newton-Raphson scheme. Secondly, a small prediction step (with a specified length) is made in the joint space of $\mathbf{z}$ and ω using the Jacobians of $\mathbf{F}$ with respect to $\mathbf{z}$ and ω. Correction steps perpendicular to the prediction step follow until the equation $\mathbf{F} = \mathbf{0}$ is fulfilled again. The sequence of prediction and correction steps are made until the highest frequency of interest is met. Since the prediction step direction and length in terms of ω is determined by the algorithm, it is possible to cross bifurcations (e.g. saddle-node bifurcations). The Jacobians of $\mathbf{F}$ are determined algebraically as far possible. Only $\partial K_\mathrm{s}/\partial|z|$, $\partial K_\mathrm{s}/\partial\omega$, $\partial F_{\mathrm{s}0}/\partial|z|$ and $\partial F_{\mathrm{s}0}/\partial\omega$ are approximated using finite difference.

5.2. Linearisation

To understand better the system dynamics, the equation of motions are linearised. This approximation is valid if the relative rotor-bearing displacements are small such that the nonlinearities of the magnetic bearings are negligible and if changes in the complex stiffness $\mathbf{K}_\mathrm{s}$ are slow compared to the rest of the system dynamics. The state $\mathbf{x}(t)$ is substituted by the complex state $\mathbf{z}(t)$ such that $\mathbf{x}(t) = \frac{1}{2}\left(\mathbf{z}(t) + \bar{\mathbf{z}}(t)\right)$. By using the same approach as in the preceding section, the linearised equation of motion becomes

$$\mathbf{M}\ddot{\mathbf{z}} + (\mathbf{C} + \omega\mathbf{G})\dot{\mathbf{z}} + (\mathbf{K} + \mathbf{K}_\mathrm{s})\mathbf{z} = \mathbf{q}_\mathrm{l}(\omega)\,\mathrm{e}^{\mathrm{i}\omega t} \tag{35}$$

Introducing $\tilde{\mathbf{z}} = \{\mathbf{z}, \dot{\mathbf{z}}\}^\intercal$, the differential equations above may be written as

$$\tilde{\mathbf{M}}\dot{\tilde{\mathbf{z}}} + \tilde{\mathbf{K}}\tilde{\mathbf{z}} = \tilde{\mathbf{q}}_\mathrm{l}(\omega)\,\mathrm{e}^{\mathrm{i}\omega t} \tag{36}$$

where

$$\tilde{\mathbf{M}} = \begin{bmatrix} \mathbf{M} & \mathbf{0} \\ \mathbf{0} & \mathbf{M} \end{bmatrix} \qquad \tilde{\mathbf{K}} = \begin{bmatrix} \mathbf{0} & -\mathbf{M} \\ \mathbf{K} + \mathbf{K}_\mathrm{s} & \mathbf{C} + \omega\mathbf{G} \end{bmatrix} \qquad \tilde{\mathbf{q}}_\mathrm{l}(\omega) = \begin{Bmatrix} \mathbf{0} \\ \mathbf{q}_\mathrm{l}(\omega) \end{Bmatrix} \tag{37}$$

The eigenstructure of the system is $-\tilde{\mathbf{M}}^{-1}\tilde{\mathbf{K}} = \mathbf{V}\boldsymbol{\Lambda}\mathbf{V}^{-1}$, where $\mathbf{V}$ contains the eigenmodes (mode shapes) and $\boldsymbol{\Lambda}$ is a diagonal matrix containing the eigenvalues (representing natural frequencies). Using the eigenstructure and $\tilde{\mathbf{z}} = \mathbf{V}\mathbf{v}$, Eq. (36) is diagonalized:

$$\dot{\mathbf{v}} = \boldsymbol{\Lambda}\mathbf{v} + \left(\tilde{\mathbf{M}}\mathbf{V}\right)^{-1}\tilde{\mathbf{q}}_\mathrm{l}(\omega)\,\mathrm{e}^{\mathrm{i}\omega t} \tag{38}$$

Note that the differential equations are independent, because $\boldsymbol{\Lambda}$ is diagonal. Equation (38) is used to explain some of the dynamic behaviour observed in the following section.

6. Results and discussion

Results of transient responses, ramp-ups and steady state frequency responses are presented below for the two system configurations using either steel or SMA springs. The configuration with steel springs is investigated at room temperature, and tests of the SMA configuration are made at 30 °C, 50 °C and 70 °C to explore the influence of temperature. Examples of applications are also presented. The system configuration with steel springs also changes its dynamic behaviour with temperature. However, tensile tests of the steel springs at different temperatures confirm that their stiffness is not temperature dependent. The changes in the system are not due to the steel springs but are caused by the stiffness of the magnetic bearings that decreases with temperature, cf. Section 4. Comparison between model predictions and experimental observations of the eigenfrequencies verifies this assumption. The changes are not significant, and in order to maintain focus on the SMAs, these results are left out.

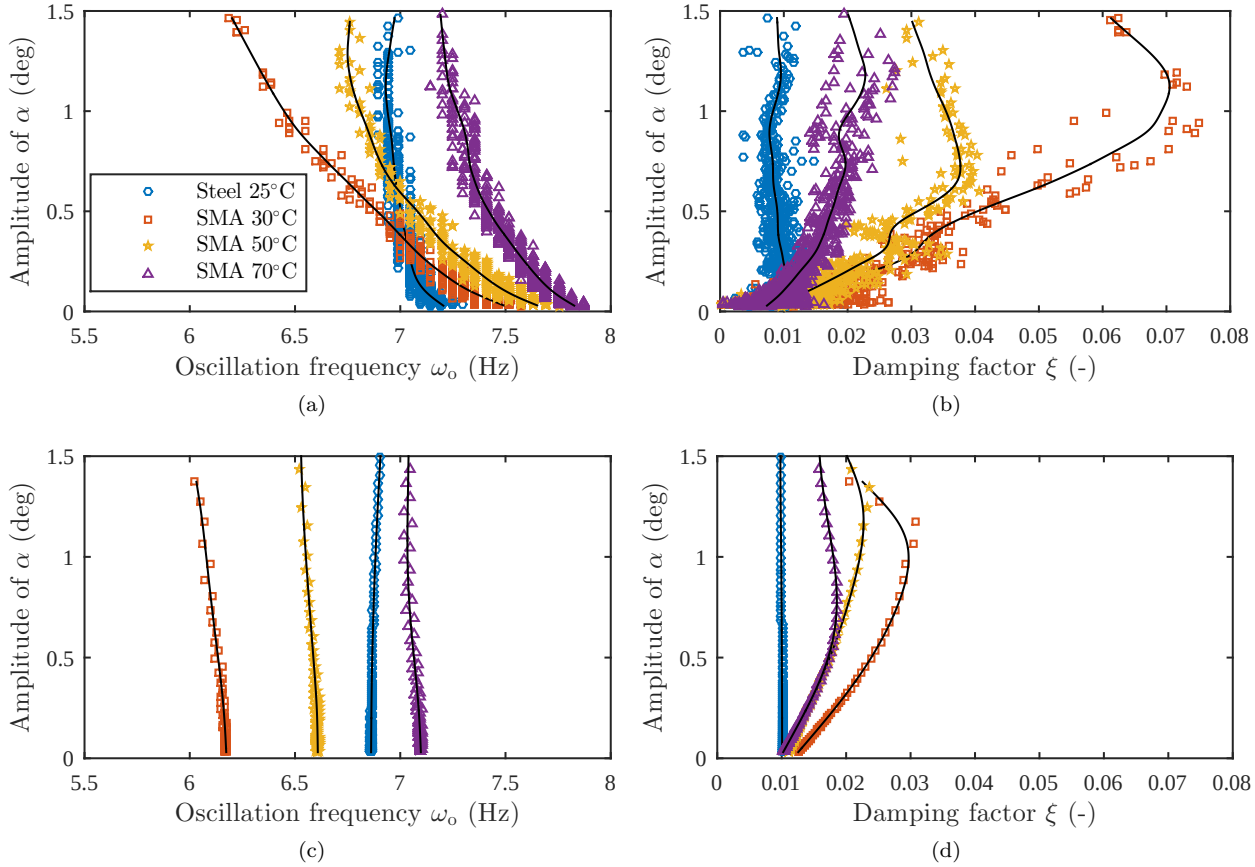

Figure 6: Oscillation frequency and damping factor depending on vibration amplitude for five different system configurations: (a) and (b) are obtained experimentally, and they are based on six tests for each system configuration, (c) and (d) are simulations. The markers are measurements, and the black lines indicate the trends and are made from smoothing splines, and they are not used for mathematical evaluation otherwise.

6.1. Transient responses

The rotor and bearing housings are released from an initial position without the rotor rotating in order to excite the lowest resonance frequency. When the rotor is not rotating, the system consists of two decoupled subsystems (α, x) and (β, y) as may be seen from the structure of the equations of motions (21). The two subsystems have two resonance frequencies each, and the first two modes consist of in-phase motion between rotor and bearing housings and the next two modes consist of counter-phase motion. It is not experimentally feasible to excite the first mode alone, and therefore a low-pass filter is used during post-processing to remove higher modes. It is important to highlight that the filtering method does not produce any phase lag. The transient responses are analysed by fitting locally in time the transient response of a linear system:

$$x(t) = x_0 \, \mathrm{e}^{-\xi\omega_\mathrm{o} t} \sin(\omega_\mathrm{o}\sqrt{1-\xi^2}t + \phi_0) \tag{39}$$

Measurement points for the fitting are obtained when the displacement reaches a maximum or minimum (corresponding to the sine factor equalling -1 or 1). Each fit is only based on three measurement points, which ensures almost perfect fits that however are subjected to measurement noise to some extent. From this, it is possible to extract the development of the oscillation frequency ω_o and the damping factor ξ as function of the amplitude $x_0 \, \mathrm{e}^{-\xi\omega_\mathrm{o} t}$ in time. The results obtained experimentally and by simulation are shown in Fig. 6 for the (α, x) subsystem.

From the experimental point of view, the system configuration with steel springs have an oscillation frequency and damping factor that are almost independent of the vibration amplitude. Therefore this system configuration behaves almost linearly. The damping factor is approximately 1 %. The SMA configuration exhibits higher level of damping: up to 7 % at 30 °C, up to 5 % at 50 °C and up to 2 % at 70 °C. Also, the oscillation frequency decreases with amplitude and increases with environmental temperature. This is typical behaviour for dynamic systems involving SMAs [33]. The frequencies of the steel configurations and the SMA configurations are close, which means the steel configuration is a valid candidate for benchmarking. If the resonance frequencies of the two configurations differed significantly, it would have a crucial impact on the mode shapes and it would not be possible to compare the results. This is also treated in the following section.

The theoretical results, Figs. 6c and 6d, are in good agreement with the experiments for the steel spring configuration. For the SMA configuration, the tendencies are similar to but not as pronounced as the experimental results. The damping factors are roughly half of the values obtained experimentally, which means that the model is conservative. The oscillation frequency decreases approximately 1.3 Hz during experiments but only 0.2 Hz in simulation for the 30 °C SMA case for example. However, in all cases there is a good agreement in frequency at high oscillation amplitudes. The discrepancies between model predictions and experimental results have several reasons: The transients obtained from experiments are filtered digitally because they originally contain more rich dynamics, which could be a source of error. Because the SMAs are hysteretic elements, their initial conditions, in terms of the martensitic volume fraction, have an impact on the dynamic response. Also, the SMA model is calibrated using data having oscillation amplitudes higher than 2 mm only, which corresponds to approximately 1°. For this reason the model cannot necessarily be expected to perform well at lower oscillation amplitudes. Finally it should be noted that differences in the necessary training process of the SMA springs that includes non-stabilized behaviour has a considerable impact on the stabilized behaviour [23]. Namely, the SMA force decreases during training, which corresponds to a fall in oscillation frequency.

The transient results for the (β, y) subsystem are very similar to the results of the (α, x) subsystem, and they are not shown here. The oscillation frequencies in (β, y) range from 7 Hz to 9 Hz and the damping factors range from 1 % to 5 %.

6.2. Ramp-ups

The rotor is accelerated from rest at 0 Hz to 20 Hz in 25 s with constant angular acceleration. The experiment is carried out four times for each system configuration with different initial rotor angles θ. Then the envelope of the rotor vibrations along time are obtained from the time signals. The results, experimental and theoretical, are shown in Fig. 7 for four different system conditions.

From the experimental results, Fig. 7a, it is clear that the system crosses four resonances resulting in four vibration peaks. The peak amplitudes and positions in time (corresponding to frequencies) depend on the system configuration and temperature. The four peak amplitudes are of the same order of magnitude. This property is due to the designed relation between the masses and the stiffnesses of the system components, which determines the (linear) mode shapes. This design has been chosen in order to make the four resonances equally important in terms of vibration reduction and also equally sensitive to the adaptive properties of the SMA springs. The high sensitivity also means that just small errors in terms of spring stiffness result in relatively large discrepancies when comparing the model prediction with the experimental results.

The experimental and theoretical results related to the steel configuration are very similar, see Figs. 7a and 7b. The peak vibration amplitudes are matched very well by the model. The tendencies related to the SMA configurations are also matched in simulation. However, the (quantitative) discrepancies are larger. The reason for this is the same as mentioned in the former section: the SMA spring forces are slightly underestimated because of differences in the training process of the springs. This results in an underestimation of the stiffness of the system, which is related to the resonance frequencies and the mode shapes and therefore also the peak amplitudes.

The SMA configuration at 30 °C has lower peak amplitudes when crossing all four resonances compared to the steel configuration. The SMA configuration at 70 °C also gives lower peaks than the steel configuration

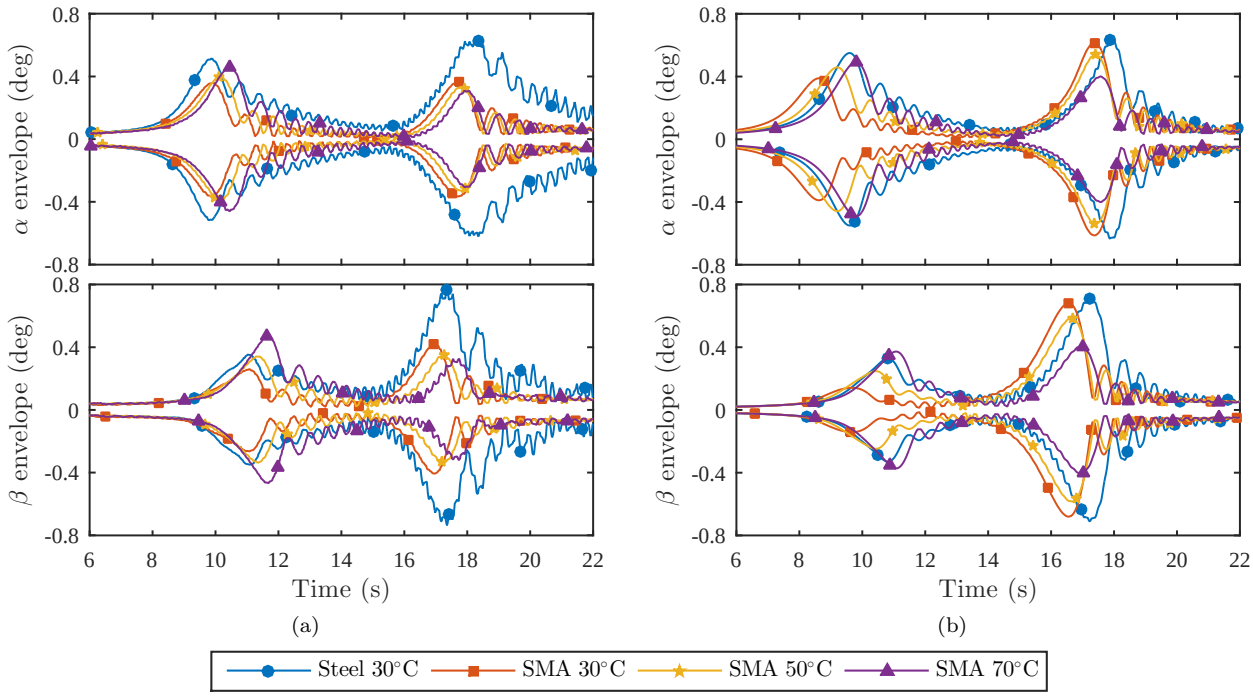

Figure 7: Experimental (a) and theoretical (b) ramp up from 0 Hz to 20 Hz in 25 s with constant acceleration using different system conditions.

in three of the resonances. It is interesting to notice that when crossing the first two resonances, the 30 °C SMA configuration performs best in terms of vibration attenuation, whereas the 70 °C configuration performs best at the two next resonances. The relation is the same in simulations, see Fig. 7b. Generally, SMAs exhibit the highest damping properties in low temperatures, which is also reflected in the loss factor shown in Fig. 3. Therefore a lower peak amplitude at 70 °C seems surprising. The reason for this behaviour is found by inspecting the linearised equations of motion in modal coordinates, Eq. (38). A change in $\mathbf{K}_s$ will affect the eigenstructure, i.e. both natural frequencies $\mathbf{\Lambda}$ and mode shapes $\mathbf{V}$. This means that there is a change of the point in time at which the peak amplitudes are reached, and it also means that there is a redistribution of the kinetic energy among the system components. Finally, a change in the mode shapes also affects how the disturbances (i.e. mass imbalance and eccentricities) influence the different modes themselves, which is seen from the last term in Eq. (38). A stiffness change causes some modes to become more sensitive or compliant to the given disturbance, and others the opposite. The effects of the change in stiffness is illustrated in Fig. 8, where the peak of the kinetic energies during a rotation cycle of the rotor and bearing housings are plotted against time for the 30 °C and 70 °C SMA conditions. The relation between the energies of the bearings and rotor clearly change when the temperature change. This corresponds to a change in mode shapes. Focusing at the two first resonances, the energies of the rotor and bearings obtained experimentally are almost identical at 30 °C. At 70 °C the kinetic energy of the rotor is significantly larger than that of the bearings. Also the sum of the kinetic energies at 70 °C are significantly larger than at 30 °C because the first two modes have become more sensitive to disturbances at high temperatures. Oppositely, the two high modes are less sensitive to the disturbances at 70 °C compared to the 30 °C case. The theoretically obtained kinetic energies show the same behaviour. Note that the energies of the first two modes are slightly underestimated and that the energies of the last two modes are overestimated which is because the average SMA stiffness is underestimated in general.

The dissipated energy by a hysteretic element is proportional to the squared vibration amplitude, the storage modulus and the loss factor. Because the storage modulus is higher at 70 °C, this means that the

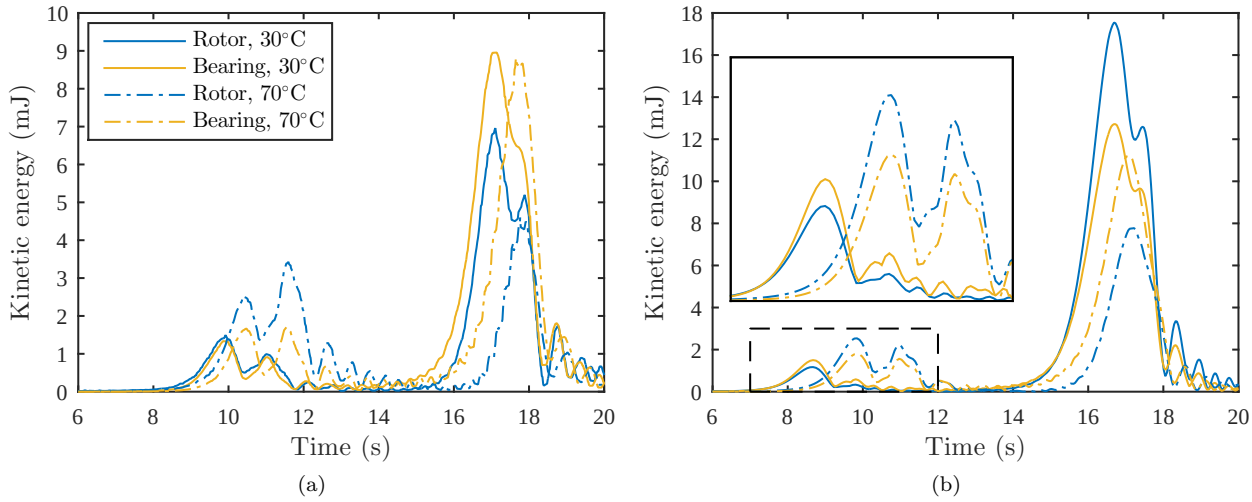

Figure 8: Peak of the kinetic energy during a rotor rotation along time during the ramp-ups shown in Fig. 7 obtained experimentally (a) and by simulation (b).

Table 3: Rotor amplitudes and frequencies of resonance peaks of the steady state frequency response related to Figs. 9 and 10. Some values are not provided because rotor-bearing impacts limit the response at the given resonance.

	Experiment				Simulation			
Mode	1, α	2, β	3, β	4, α	1, α	2, β	3, β	4, α
Amplitude (°)								
Steel 30 °C	1.04	0.97	–	0.67	1.34	0.75	–	–
SMA 30 °C	0.46	0.32	0.63	0.64	0.55	0.22	0.91	0.77
SMA 50 °C	0.55	0.42	0.54	0.60	0.70	0.39	0.77	0.68
SMA 70 °C	0.82	0.70	0.52	0.58	0.75	0.54	0.56	0.50
Frequency (Hz)								
Steel 30 °C	7.0	7.9	–	13.7	6.9	7.8	–	–
SMA 30 °C	6.9	7.9	12.8	13.5	6.1	7.0	12.8	13.3
SMA 50 °C	7.2	8.1	12.9	13.6	6.6	7.5	12.8	13.3
SMA 70 °C	7.4	8.4	13.3	13.8	7.1	8.1	12.9	13.4

actual damping capacity is only reduced slightly compared to at 30 °C at this level of vibration amplitudes, cf. Fig. 3.

6.3. Steady state responses

The system is kept at a constant rotational frequency and the responses in terms of rotor and bearing housing vibration amplitude and phase are captured, when a steady state is reached. A small change is made to the frequency and the procedure is repeated. The analysis is performed in the frequency range from $\omega = 1$ Hz to $\omega = 20$ Hz, wherein the interesting system dynamics take place. Both an up-sweep and a down-sweep are performed in order to explore jumps between co-existing stable states. The experimental results in the frequency ranges close to resonance conditions may be seen in Fig. 9 for the steel configuration at room temperature and the SMA configuration at three temperature levels. Resonance peak vibration amplitudes and frequencies of the rotor are provided in Tab. 3.

From the figure it is possible to observe the four resonance conditions. For the SMA configurations the two first resonances (around 7 and 8 Hz) are characterized by slightly asymmetric resonance peaks bending towards the left because of softening. As mentioned before the softening behaviour is typical for

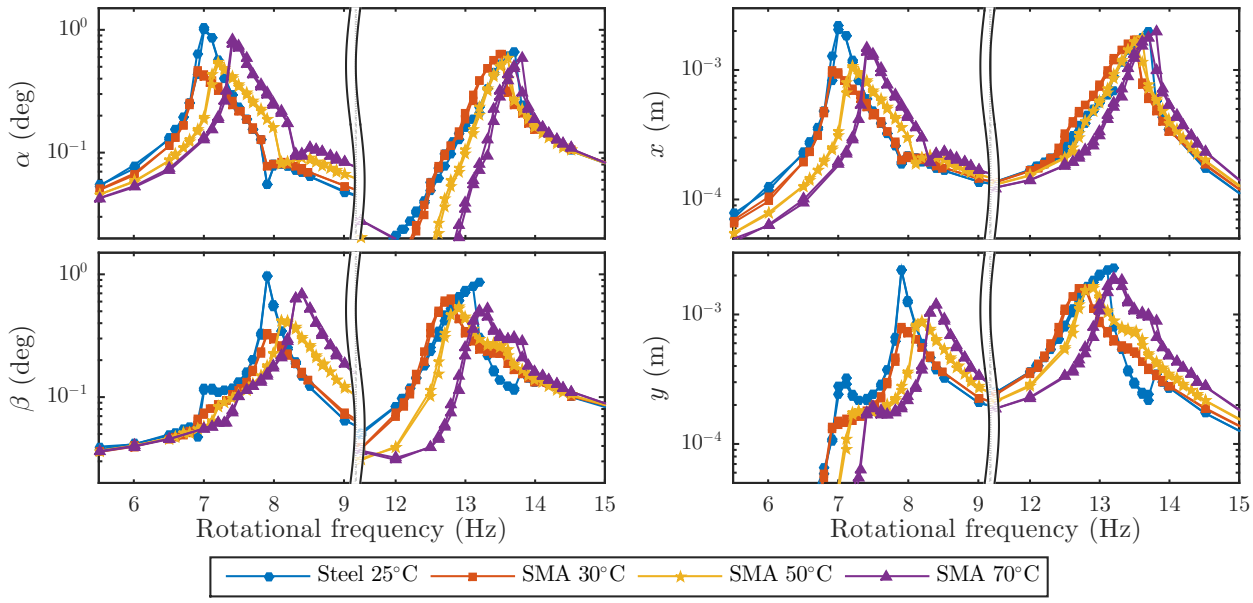

Figure 9: Experimentally obtained amplitude of the fundamental harmonic response at different constant rotational frequencies.

SMA systems, and it is in agreement with the transient results presented in Section 6.1. The two highest resonances (around 13 Hz) are almost coinciding and they are characterized by stiffening in all system conditions. In the steel configuration and in the 50 °C and 70 °C SMA cases it is possible to observe co-existing states and jump phenomena. Since the stiffening is found both with and without SMAs, it is evident that the SMAs are not responsible for this behaviour. The effect is caused by the magnetic bearings that are weakly nonlinear with stiffening, cf. Section 4. The influence of the magnetic bearing stiffening is particularly significant in the two highest resonances because of counter-phase motion between the rotor and the bearing housings resulting in large relative vibration amplitudes. The peak amplitudes of the steel configurations are larger than those of the SMA configuration in all resonances and temperatures. Actually, rotor-bearing impacts occur when trying to sweep up across the two highest resonances in the steel case. The four resonance frequencies increase with temperature using the SMA configuration. The first three increase by 0.5 Hz and the fourth increase by 0.3 Hz comparing 70 °C to 30 °C, which correspond to 7 %, 6 %, 4 % and 2 % respectively. The peak vibration amplitudes also increase with temperature at the first two critical speeds for all states (both rotor and bearings). However, at the two next critical speeds the peak amplitudes of the rotor (α and β) decrease with temperature, whereas the situation is the opposite for the bearing housings (x and y). The rotor peak amplitudes at the two first resonances are reduced by 43 % and 54 % respectively by decreasing the temperature from 70 °C to 30 °C. For the third and fourth resonances the peaks are reduced by 17 % and 9 % respectively by increasing the temperature from 30 °C to 70 °C. The observations are in agreement with the ramp-up results presented in the former section.

The frequency responses are also obtained theoretically with the use of the approximative model described in Section 5.1. The results may be seen in Fig. 10. The resemblance to the experimental results is good. The two first resonances are characterized by light softening and the two highest by stiffening. The steel configurations exhibit the highest peak amplitudes. The peak amplitudes of the two first resonances increase with SMA temperature for all states, but it is a mixture at the two highest resonances. By using the continuation technique, it is also possible to discover the unstable branches when crossing the saddle-node bifurcations close to the third and fourth resonances. Using the model, it is confirmed that the stiffening effect characterizing the two highest resonances completely vanish, if the nonlinearity of the magnetic bearings is omitted. The magnetic nonlinearity is therefore the only cause for the right bending of the third and fourth resonance peaks.

Because the continuation method is applied to an approximation of the model, justification is needed.

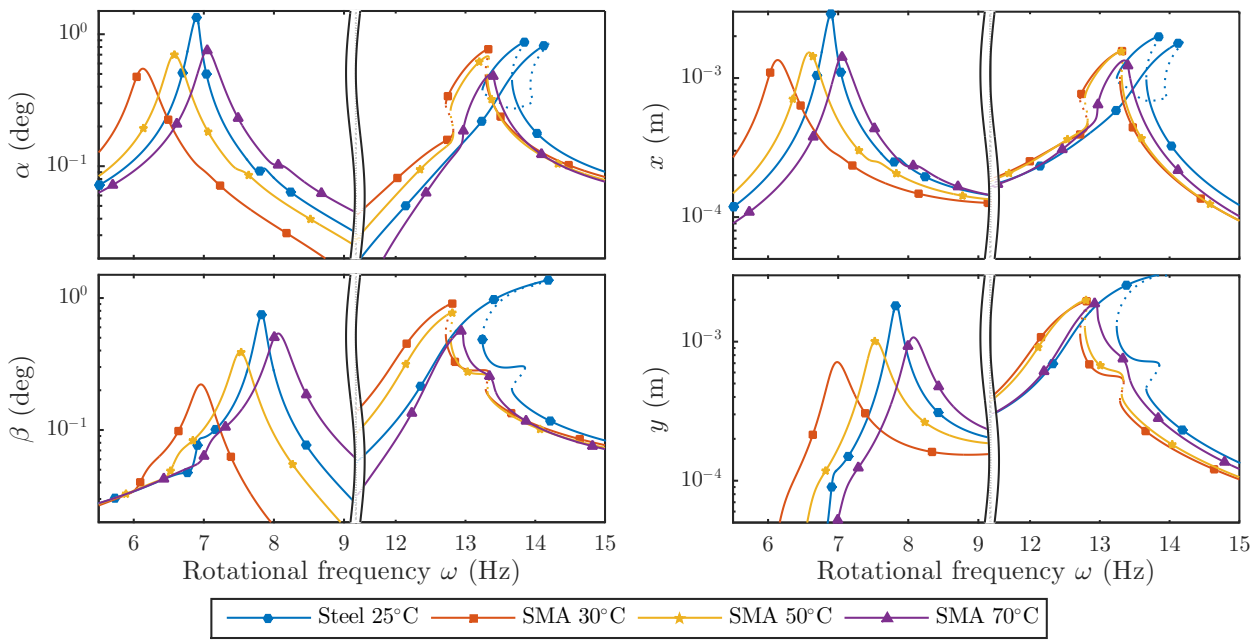

Figure 10: Frequency responses of the rotor obtained using pseudo-arclength continuation of the approximative equations of motion in frequency domain giving the amplitude of the fundamental harmonic content for different rotational frequencies. Dotted lines indicate unstable branches.

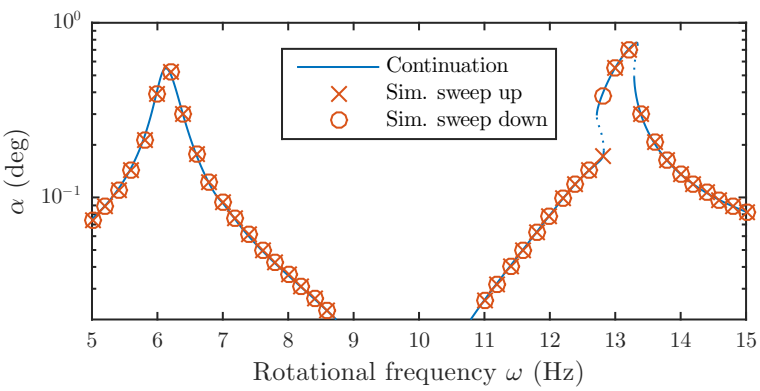

Figure 11: Comparison between results obtain via continuation of approximative model and simulations (sweep up or sweep down) of full model. The amplitude of the fundamental harmonic content is shown.

For this reason time simulations of the full model are compared to the results obtained via continuation. An example is shown in Fig. 11. The graph shows a complete match between the two approaches. The continuation results can be obtained within seconds, whereas the simulations take several minutes. More importantly, the continuation method provides more rich information about the system dynamics in form of higher resolution and unstable branches, which cannot be obtained via time simulation. It is important to mention that a Fourier transform of the steady state solutions obtained via time simulation reveals that no sub-harmonics are present and that super-harmonics are at least two orders of magnitude lower than the fundamental harmonic. The simplification of only allowing the fundamental harmonic is therefore reasonable.

6.4. Applications

Based on the presented experimental and theoretical results it is evident that the SMA configuration of the system is adaptable through temperature control. Here examples are presented related to open loop control of the temperature with the aim of reducing rotor vibrations. Figure 12 shows three cases, in which the rotational speed is kept constant at different levels. Both experimental and theoretical results are shown. To illustrate the same qualitative behaviour, the theoretical operational speeds are altered slightly compared to the experimental speeds, because the resonance frequencies differ slightly between the experiments and the model.

In the first case, Figs. 12a (experiment) and 12b (simulation), the operational speed is close to the second critical speed at 70 °C. Instead of changing the operational speed, it is possible to move away the critical speed by decreasing the temperature of the SMA springs. At $t = 200$ s, when the SMA environmental temperature is close to 30 °C, the vibration amplitude is reduced approximately 75 % in the β direction of the experiments. The α direction is only affected to small extent. The theoretical results show the same tendency. Both the initial and final vibration amplitudes are smaller compared to the experiments, and the reduction is around 95 %.

The second case, Figs. 12c (experiment) and 12d (simulation), starts just below the second critical speed at 70 °C. In this case, the critical speed moves closer to the rotational speed when decreasing the SMA temperature to 50 °C thus resulting in vibration amplification in the β direction. However, vibrations in the α direction are reduced. By further reducing the SMA temperature to 30 °C, the second critical speed moves away from the operational speed and vibrations in β reduce. Therefore, the overall vibrations are reduced when taking both α and β into account. The theoretical results are very similar. This example also shows the potential of crossing a critical speed by a change in temperature instead of ramping up. This approach has been proposed by several authors [2, 3, 7, 8, 16, 34, 35]. The idea is to "jump" directly from high temperature (70 °C) to low temperature (30 °C) and thus avoid exciting the mode that is crossed. However, it is not possible to jump directly because the changes in temperature are slow (in the order of 10 s) as may be seen from the experimental results, and it is inevitable to avoid exciting the mode as a result. It is therefore important to have considerable dissipation in the system to reduce the peak amplitude when crossing the critical speed and to attenuate subsequent transients. The decrease of SMA stiffness due to the temperature fall is clearly visible when plotting the SMA forces against the bearing housing displacement, Fig. 13a. Only at 50 °C it is possible to observe small amounts of hysteresis. The hysteresis is therefore not present in the optimal conditions, in which the vibrations are small. The hysteresis is only useful for limiting large vibrations.

The system is close to its fourth critical speed at 30 °C in Figs. 12e and 12f. Here, vibrations in α are large. In order to reduce the vibrations the temperature is increased. However, this means that the third critical speed related to the β direction comes closer. In order to reduce the overall vibrations, an intermediate state close to 50 °C could therefore be understood as an optimum. This highlights that it may be useful to have a continuous temperature interval at disposal and not only "cold" and "hot" conditions in order to obtain optimal conditions. This can also be used to tune anti-resonances close to the operational speed [7, 11]. Figure 13b shows the simulated SMA forces against the bearing housing displacement related to the case in Figs. 12e and 12f. The SMA stiffness clearly increases with temperature in both x and y. There is significant hysteresis at 30 °C in the x direction where vibrations are large. On the other hand, the vibration amplitudes of α and x are smallest at 70 °C, at which there is no hysteresis in the x direction.

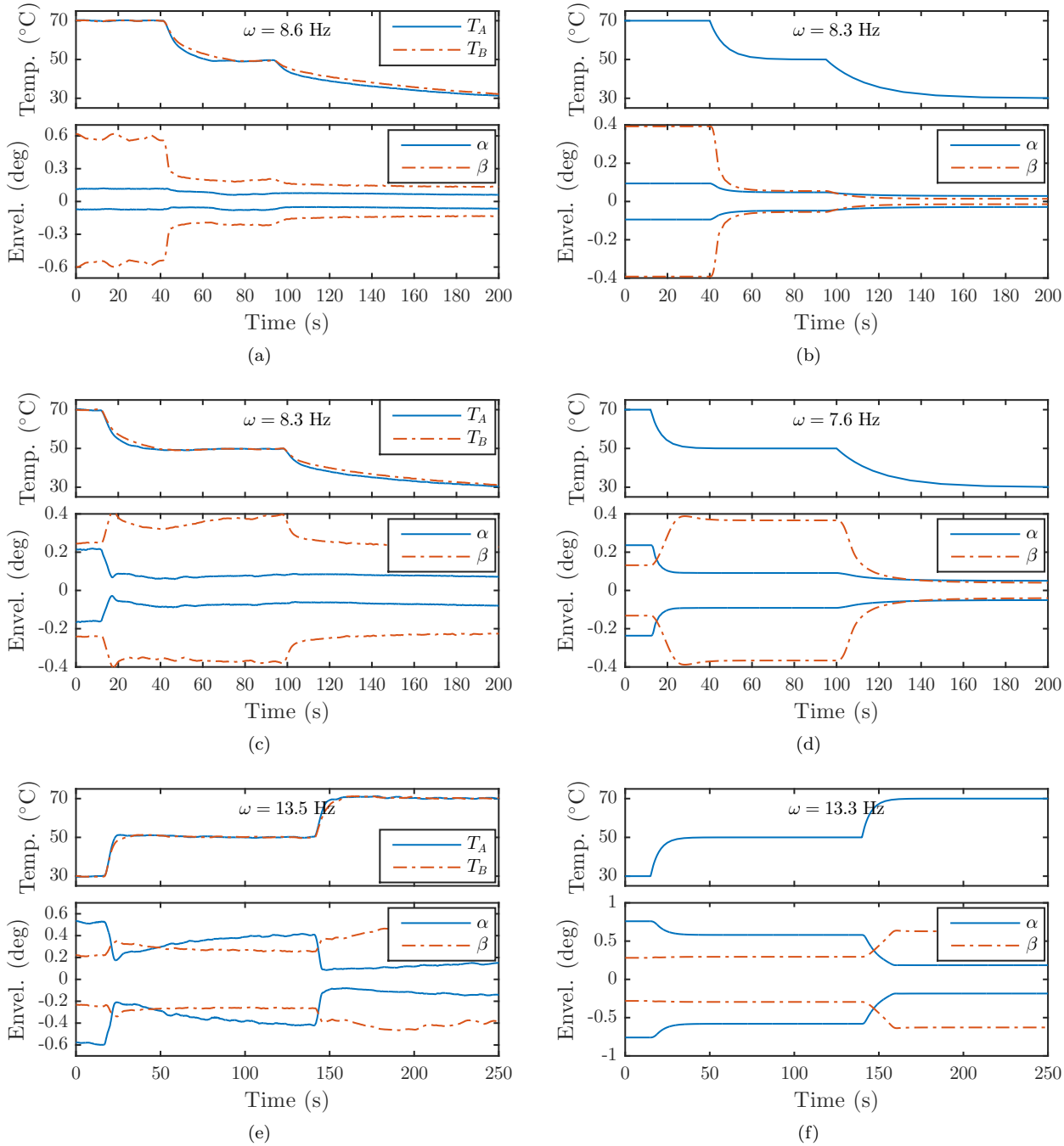

Figure 12: Examples of applications related to temperature control of SMAs in the rotor-bearing systems at constant rotational speeds. There are three pairs consisting of experimental results (a), (c) and (e) followed by numerical simulations (b), (d) and (f). Environmental temperatures are plotted together with the envelope of rotor vibrations. In experiments T_A denotes the temperatures of the heat chambers located at the positive X and Y faces of the upper bearing, and T_B for the negative X and Y faces. In simulations the temperatures are equal.

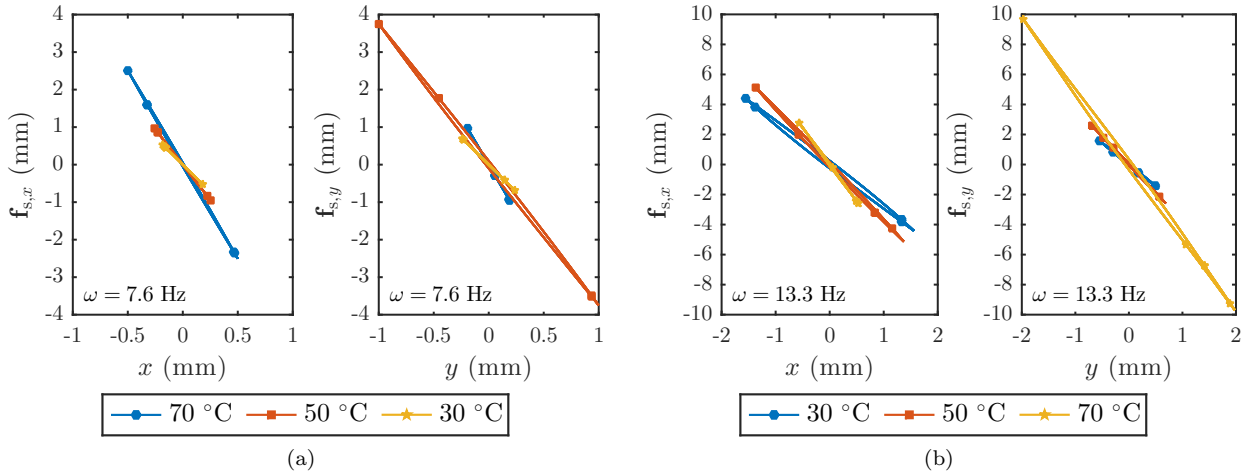

Figure 13: Simulated SMA forces against bearing housing displacement during steady state conditions. (a) corresponds to Fig. 12d and (b) to Fig. 12f.

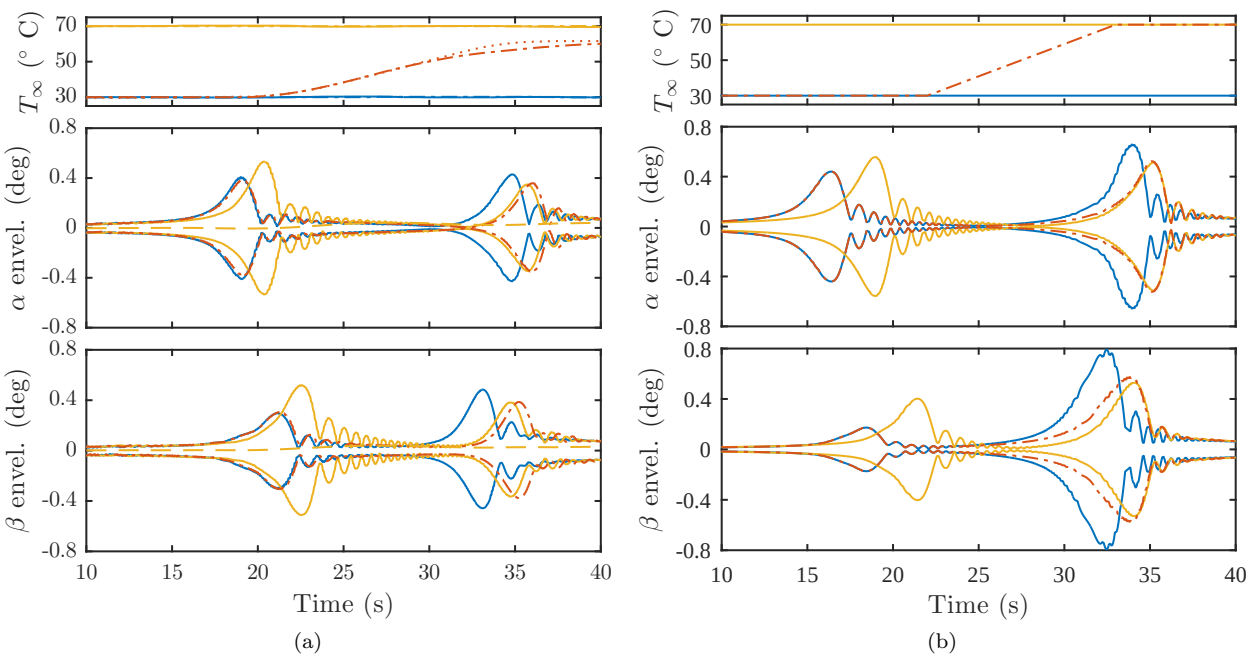

Figure 14: Experimental (a) and theoretical (b) ramp ups from 0 Hz to 20 Hz in 50 s with constant acceleration using either constant (blue and yellow) or time varying (red) SMA environment temperatures. The heat chamber temperatures and the envelope of the rotor vibrations are shown.

Section 6.2 highlighted ramp-ups of the system with different SMA temperatures. We concluded that the smallest peak amplitudes are obtained at 30 °C when crossing the first two critical speeds and at 70 °C when crossing the third and fourth critical speeds. In order to reduce the overall vibrations during a ramp-up, it is therefore necessary to change the SMA temperature during the process. This aspect is shown in Figs. 14a and 14b for experiments and simulation respectively. Here three cases are compared, in which the SMA environment temperature is either 30 °C, 70 °C or changes over time. In the third case, the temperature is 30 °C when crossing the first two resonances, and the response is therefore close to the static 30 °C case. Around $t = 20$ s the reference of the temperature controller is set to 70 °C. When the system crosses the third and fourth critical speeds the system has changed its characteristics, and the response therefore follows the static 70 °C case. This way the overall vibrations are minimized.

As shown in Figs. 12c and 12d, it is also possible to pause during a ramp-up just before a resonance and then cross it by a temperature change and afterwards continue ramping. However, this approach is not useful in terms of vibration attenuation for this system: Even though the environmental temperature of the heat chamber is altered instantaneously, the SMA springs still uses around five seconds to drop from 70 °C to 30 °C because of their heat capacity, which can be predicted by the model. The shift in temperature is therefore not instantaneous and transients have time to build up. Secondly, by using a temperature shift it would mean that the resonance is encountered at an intermediate temperature. As shown before, it is best to cross a resonance at either the lowest and highest temperature, and not at an intermediate temperature, depending on the resonance in question. Finally, because the system resonances are closely spaced in pairs and because the temperature controller does not control the SMA springs individually but together, it is complex to determine an optimal temperature path.

7. Conclusions

A rotor-bearing system having four degrees of freedom (rotor tilt and bearing housing lateral motion) is investigated theoretically and experimentally. The upper bearing housing is suspended by four helical springs made from either steel or a pseudoelastic SMA. The steel configuration of the system is used as benchmark so the performance of the SMAs can be quantified. Large extents of the system have linear characteristics, but the passive magnetic bearings contain weak nonlinearities with stiffening, and also the SMA springs behave weakly nonlinearly depending on strain rate, stoke length and temperature. The combination of the linear parts and the weak nonlinearities governs the system dynamics.

Transient responses of the system with SMA suspension excited in its first mode show that the oscillation frequency as well as damping characteristics depend on the vibration amplitude. The damping, which is related to mechanical hysteresis in the SMA springs, is highest at high amplitudes and low temperatures. The damping factor is up to seven times higher than that of the steel configuration based on experimental results, whereas numerical simulations of the system gives a factor of three. Also the vibration frequency vary with the SMA temperature (up to 7 %) defining the system adaptability, and it also varies with vibration amplitude (softening). This is confirmed by the model even though the dependencies are not as pronounced as in experiments. Both experiments and simulations show reductions in the order of 50 % during ramp-up of the system.

A change in the environmental temperature of the SMA springs has several implications for the system dynamics: The resonance frequencies and the mode shapes change. This means that the distribution of energy among the system components is affected and it also affects the sensitivities to disturbances (e.g. imbalance) of the different modes. For these reasons, the rotor peak amplitude actually decreases with temperature when crossing the third and fourth modes even though the hysteresis diminishes. In order to achieve this kind of behaviour, a holistic approach is required during the design phase, meaning that the SMA machine elements and the rest of the system components (i.e. masses and stiffnesses) are treated simultaneously.

Steady state frequency responses are obtained experimentally and also theoretically via an approximative model using continuation techniques. Comparison between time simulations and continuation results confirms that the assumptions used in the approximative model are valid, the main assumption being that the steady state system response only contains the fundamental frequency of the excitation thus being simple

harmonic. Therefore the system does not show any strong nonlinear behaviour. The steady state frequency responses also show slight softening of the two first resonances and clear stiffening of the third and fourth resonances resulting in jump phenomena and co-existing states. The slight softening is due to the SMA springs, and the stiffening behaviour is solely due to the nonlinearities of the magnetic bearings and is not related to the SMAs.

Vibration attenuation during constant rotational speed can also be achieved by changing the environmental temperature of the SMAs. The optimal SMA temperature depends on the operational speed. Large vibration attenuations are primarily caused by changes in the resonance frequencies, which move relative to the operational frequency. The consequent changes in mode shapes, mode sensitivity and damping capacity due to hysteresis are only secondary factors. The hysteresis only works at high vibration amplitudes and therefore only limits large vibrations and do not define optimal conditions.

Acknowledgement

The Danish Ministry of Science, Innovation and Higher Education provided funding for the FTP Research project 12-127502. We thank Prof. Marcelo A. Savi from Federal University of Rio de Janeiro for some fruitful discussions.

References

[1] C. Liang, C. A. Rogers, Design of shape memory alloy springs with applications in vibration control, Journal of Vibration and Acoustics 115 (1) (1993) 129–135. doi:10.1115/1.2930305.

[2] K. Nagaya, S. Takeda, Y. Tsukui, T. Kumaido, Active control method for passing through critical speeds of rotating shafts by changing stiffnesses of the supports with use of memory metals, Journal of Sound and Vibration 113 (2) (1987) 307–315. doi:10.1016/S0022-460X(87)80217-1.

[3] J. Nie, X. Yan, Intelligent bearing system for passing through critical speed of aeroengine rotor by changing stiffness using SMA wires, Materials Science Forum 327-328 (2000) 99–102. doi:10.4028/www.scientific.net/MSF.327-328.99.

[4] A. W. Lees, S. Jana, D. J. Inman, M. P. Cartmell, The control of bearing stiffness using shape memory, in: The Society for Experimental Mechanics Series, 2007.

[5] A. J. Żak, M. P. Cartmell, W. M. Ostachowicz, Dynamics and control of a rotor using an integrated SMA/composite active bearing actuator, Key Engineering Materials 245-246 (2003) 233–240. doi:10.4028/www.scientific.net/KEM.245-246.233.

[6] D. J. Inman, M. P. Cartmell, A. W. Lees, T. Leize, L. Atepor, Proposals for controlling flexible rotor vibrations by means of an antagonistic SMA/composite smart bearing, Applied Mechanics and Materials 5-6 (2006) 29–36. doi:10.4028/www.scientific.net/AMM.5-6.29.

[7] Y.-Y. He, S. Oi, F.-L. Chu, H.-X. Li, Vibration control of a rotor-bearing system using shape memory alloy: I. Theory, Smart Materials and Structures 16 (1) (2007) 114–121. doi:10.1088/0964-1726/16/1/014.

[8] Y.-Y. He, S. Oi, F.-L. Chu, H.-X. Li, Vibration control of a rotor-bearing system using shape memory alloy: II. Experimental study, Smart Materials and Structures 16 (1) (2007) 122–127. doi:10.1088/0964-1726/16/1/015.

[9] J. M. Borges, A. A. Silva, C. J. de Araújo, E. d. M. Fernandes, R. L. Pimentel, A. A. Santiago, Rotor-bearing vibration control system based on fuzzy controller and smart actuators, International Journal of Multiphysics 7 (3) (2013) 197–205. doi:10.1260/1750-9548.7.3.207.

[10] M. T. S. Alves, S. Enemark, V. Steffen Jr, I. F. Santos, Vibration control of a flexible rotor using shape memory alloy wires, in: The XVII International Symposium on Dynamic Problems of Mechanics, 2015.

[11] S. Enemark, I. F. Santos, M. A. Savi, Shape memory alloys applied to improve rotor-bearing system dynamics – an experimental investigation, in: The XVII International Symposium on Dynamic Problems of Mechanics, 2015.

[12] L. C. Silva, M. A. Savi, A. Paiva, Nonlinear dynamics of a rotordynamic nonsmooth shape memory alloy system, Journal of Sound and Vibration 332 (3) (2013) 608–621. doi:10.1016/j.jsv.2012.09.018.

[13] E. Sitnikova, E. Pavlovskaia, M. Wiercigroch, M. A. Savi, Vibration reduction of the impact system by an SMA restraint: numerical studies, International Journal of Non-Linear Mechanics (2010) 1–13doi:10.1016/j.ijnonlinmec.2009.11.013.

[14] B. Ertas, H. Luo, D. Hallman, Dynamic characteristics of shape memory alloy metal mesh dampers, in: Structures, Structural Dynamics, and Materials and Co-located Conferences, American Institute of Aeronautics and Astronautics, 2009. doi:10.2514/6.2009-2521.

[15] Y. Ma, Q. Zhang, D. Zhang, F. Scarpa, B. Liu, J. Hong, A novel smart rotor support with shape memory alloy metal rubber for high temperatures and variable amplitude vibrations, Smart Materials and Structures 23 (12) (2014) 125016. doi:10.1088/0964-1726/23/12/125016.

[16] Y. Ma, Q. Zhang, D. Zhang, F. Scarpa, B. Liu, J. Hong, Tuning the vibration of a rotor with shape memory alloy metal rubber supports, Journal of Sound and Vibration 351 (2015) 1–16. doi:10.1016/j.jsv.2015.04.005.

[17] D. Bernardini, G. Rega, Thermomechanical modelling, nonlinear dynamics and chaos in shape memory oscillators, Mathematical and Computer Modelling of Dynamical Systems 11 (3) (2005) 291–314. doi:10.1080/13873950500076404.

[18] M. A. Savi, A. S. De Paula, D. C. Lagoudas, Numerical investigation of an adaptive vibration absorber using shape memory alloys, Journal of Intelligent Material Systems and Structures 22 (1) (2011) 67–80. doi:10.1177/1045389X10392612.

[19] E. Sitnikova, E. Pavlovskaia, J. Ing, M. Wiercigroch, Suppressing nonlinear resonances in an impact oscillator using SMAs, Smart Materials and Structures 21 (7) (2012) 075028. doi:10.1088/0964-1726/21/7/075028.

[20] M. Piedboeuf, R. Gauvin, M. Thomas, Damping behaviour of shape memory alloys: strain amplitude, frequency and temperature effects, Journal of Sound and Vibration 214 (5) (1998) 885–901. doi:10.1006/jsvi.1998.1578.

[21] F. Gandhi, D. Wolons, Characterization of the pseudoelastic damping behavior of shape memory alloy wires using complex modulus, Smart Materials and Structures 8 (1) (1999) 49–56. doi:10.1088/0964-1726/8/1/005.

[22] S. A. Holanda, A. A. Silva, C. J. de Araujo, A. S. de Aquino, Study of the complex stiffness of a vibratory mechanical system with shape memory alloy coil spring actuator, Shock and Vibration 2014 (2014) Article ID 162781. doi:10.1155/2014/162781.

[23] S. Enemark, I. F. Santos, M. A. Savi, Characterisation, modelling and uncertainties of rate-dependent pseudoelastic shape memory alloy helical springs, Journal of Intelligent Material Systems and Structures, accepted.

[24] M. Krack, J. Böttcher, A method for the computational assessment of the damping performance of shape-memory alloys, Smart Materials and Structures 23 (8) (2014) 085010. doi:10.1088/0964-1726/23/8/085010.

[25] K. A. Williams, G. T.-C. Chiu, R. J. Bernhard, Feedback control of an active material adaptive tuned vibration absorber using relative phase, in: SPIE, Smart Structures and Materials 2002: Smart Structures and Integrated Systems, Vol. 4701, 2002, pp. 200–213. doi:10.1117/12.474659.

[26] D. C. Lagoudas, D. Hartl, Y. Chemisky, L. Machado, P. Popov, Constitutive model for the numerical analysis of phase transformation in polycrystalline shape memory alloys, International Journal of Plasticity 32–33 (2012) 155–183. doi:10.1016/j.ijplas.2011.10.009.

[27] A. M. Wahl, Mechanical springs, first edition Edition, Penton Publishing Co., Cleveland, 1944.

[28] D. Wolons, F. Gandhi, B. Malovrh, Experimental investigation of the pseudoelastic hysteresis damping characteristics of shape memory alloy wires, Journal of Intelligent Material Systems and Structures 9 (2) (1998) 116–126. doi:10.1177/1045389X9800900205.

[29] J. R. Banerjee, D. Kennedy, Response of an axially loaded timoshenko beam to random loads, Journal of Sound and Vibration 101 (4) (1985) 481–487.

[30] S. Enemark, I. F. Santos, Nonlinear dynamic behaviour of a rotor-foundation system coupled through passive magnetic bearings with magnetic anisotropy – Theory and experiment, Journal of Sound and Vibration, in pressdoi:10.1016/j.jsv.2015.10.007.

[31] D. K. Cheng, Field and Wave Electromagnetics, Addison-Wesley Publishing Company, Reading, Massachusetts, 1983.

[32] A. H. Nayfeh, B. Balachandran, Applied nonlinear dynamics. Analytical, computational, and experimental methods, John Wiley & Sons, Inc., New York, 1995.

[33] R. A. A. Aguiar, M. A. Savi, P. M. C. L. Pacheco, Experimental investigation of vibration reduction using shape memory alloys, Journal of Intelligent Material Systems and Structures 24 (2) (2013) 247–261. doi:10.1177/1045389X12461696.

[34] K. Gupta, A. K. Darpe, B. Kumar, A. Bhatia, S. M. Ahmed, T. S. Aravindhan, B. C. Nakra, Resonance control of rotor using shape memory alloys, Advances in Vibration Engineering 8 (3) (2009) 247–254.

[35] T. S. Aravindhan, K. Gupta, Multiple smart material applications using SMA and MR fluid damper for rotor vibration control, in: The ASME Turbo Expo 2010: Power for Land, Sea and Air, Vol. 6, American Society of Mechanical Engineers, 2010, pp. 299–308. doi:10.1115/GT2010-23084.